

# A mineral magnetic characterization of the Plio-Pleistocene fluvial infill of the Heidelberg Basin (Germany)

Stephanie Scheidt,<sup>1,2</sup> Ramon Egli,<sup>3</sup> Thomas Frederichs,<sup>4</sup> Ulrich Hambach<sup>2,5,6</sup> and Christian Rolf<sup>1</sup>

<sup>1</sup>Leibniz Institute for Applied Geophysics, D-30655 Hannover, Germany. E-mail: [stephanie.scheidt@liag-hannover.de](mailto:stephanie.scheidt@liag-hannover.de)

<sup>2</sup>Chair of Geomorphology, University of Bayreuth, D-95440 Bayreuth, Germany

<sup>3</sup>Central Institute for Meteorology and Geodynamics, 1190 Vienna, Austria

<sup>4</sup>Faculty 5 Geosciences, University of Bremen, D-28334 Bremen, Germany

<sup>5</sup>BayCEER, University of Bayreuth, D-95440 Bayreuth, Germany

<sup>6</sup>Laboratory for Palaeoenvironmental Reconstruction, Faculty of Sciences, University of Novi Sad, 21000 Novi Sad, Serbia

Accepted 2017 April 18. Received 2017 April 10; in original form 2017 January 13

## SUMMARY

The Heidelberg Basin (Germany) hosts a quasi-continuous sedimentary sequence of primarily fluvial sediments with pedogenetic overprints and lacustrine intercalations. This unconsolidated succession has been shown to record a consistent magnetic polarity stratigraphy of the Quaternary and the late Neogene. Previous work has reported that sulphides and high-coercive minerals are the carriers of the remanent magnetization. Here, we provide the results of an extended mineral magnetic study that aims to disentangle the complex magnetic mineralogy. In addition, we assess the reliability of these minerals as carriers of palaeomagnetic signals. A major obstacle to the analysis of the drill cores was the large number of samples that were taken from a total core length of 1150 m. Rapid measurements on bulk samples provided only limited information on the magnetic mineralogy. In contrast, time-intensive methods such as first-order reversal curves (FORCs) or coercivity analyses, for example, yielded valuable information. The combined results of all the analyses consider the heterogeneous compositions of the sediments and indicate a varying palaeoenvironmental history. The Pliocene Iffezheim Formation was formed under alternating reducing and oxidizing conditions. Magnetite, maghemite, haematite and goethite are the predominant magnetic minerals. Sulphides were only preserved under specific conditions. The Pleistocene sediments reflect predominantly reducing conditions during sedimentation and diagenesis. Greigite, pyrite and most likely pyrrhotite have been shown to occur. Taken together, our work provides a detailed environmental magnetic record of the Plio-Pleistocene and elucidates the capabilities and limitations of rock magnetic studies performed on fluvial dominated sedimentary successions.

**Key words:** Europe; Environmental magnetism; Magnetic mineralogy and petrology; Rock and mineral magnetism.

## 1 INTRODUCTION

Rock magnetic analyses of sediment deposits represent well-established techniques for reconstructing environmental processes. A large number of studies used these techniques to examine deep-sea sediments (Robinson 1986; Bloemendal *et al.* 1992), loess (Heller & Liu 1986; Liu *et al.* 1993; Liu *et al.* 2007) and lacustrine sediments (Dearing 1999; Nowaczyk 2011). In many cases, these sediments contain well-defined magnetic mineral components and provide a minimum degree of continuity and relatively monotonous sedimentation mechanisms in (long-term) stable environments. An increasing number of studies on more complex

systems have emerged during the last few decades. Such systems include tectonically disturbed sequences, sediments with unusual magnetic mineral assemblages, and remagnetized or diagenetically overprinted rocks (e.g. Hallam & Maher 1994; Hounslow 1996; Biswas *et al.* 1999; Maher & Hallam 2005; Horng & Roberts 2006; Rowan & Roberts 2006; Lucifora *et al.* 2012). Despite these advances, unconsolidated fluvial sediments are still seldom the focus of rock magnetic research. Fluvial deposits are characterized by laterally and vertically irregular distributions of sedimentary bodies with interposed hiatuses of unknown durations. Variations in the primary mineralogical composition of fluvial sediments are influenced by a wide variety of factors, including changes in source

areas, changes in the size and base level of the river catchment and the number of tributaries it contains, and regional subsidence. Additionally, erosion, abrasion, inundation, and transportation processes have direct effects on the sedimentary architecture and composition of deposits (Miall 2013). Further, hydrological conditions and climatic aspects, particularly seasonal variations, can lead to cyclic changes in sediment input and to alternations between oxidizing and reducing conditions. Finally, in situ weathering and diagenesis affect sedimentary bodies and can cause the (partial) dissolution and alteration of existing magnetic components, as well as the formation of new minerals (Roberts 2015). Therefore, natural fluvial sediments contain heterogeneous mixtures of magnetic minerals and display small-scaled variations in the temporal and spatial distribution patterns. Despite the considerable complexity of fluvial deposits, a small number of magnetostratigraphic and palaeomagnetic studies have demonstrated that meaningful results can be obtained (e.g. Johnson *et al.* 1986; Hounslow *et al.* 1995; Kempf *et al.* 1999; Scardia *et al.* 2006; Scheidt *et al.* 2015).

In this paper, we present the results of a detailed rock magnetic analysis of fluvial sediments from the Heidelberg Basin, which hosts one of the thickest continental Plio-Pleistocene sedimentary successions in central Europe (Gabriel *et al.* 2008). A magnetostratigraphic age model for this basin has been obtained by Scheidt *et al.* (2015) from simple piecewise linear interpolation of age tie points corresponding to magnetic polarity changes. In this paper, we present the results of detailed rock magnetic investigations of 1150 m of core material from three sites, based on hysteresis and FORC measurements and high-temperature measurements, as well as principal component analyses of isothermal remanent magnetization (IRM) acquisition curves. The rock magnetic measurements are complemented by scanning electron microscopy (SEM) and energy-dispersive X-ray microanalysis (EDX). To our knowledge, this is the first integrated study of such an extensive set of samples from fluvial sediments, and it provides deeper insight into the magnetic mineralogy of unconsolidated riverine deposits. Furthermore, the results of this study support the magnetostratigraphic model of Scheidt *et al.* (2015), providing a solid base for a model of Pliocene and Pleistocene palaeoenvironmental evolution within the region (Scheidt *et al.*, in preparation).

## 2 GEOLOGICAL SETTING, CORES AND SAMPLES

The Heidelberg Basin is part of the northern Upper Rhine Graben (URG) in Germany. Continuous subsidence started in the late Oligocene (Schumacher 2002) and led to accumulation of sedimentary sequences that are more than 2000 m in thickness at the location of the modern city of Heidelberg (Buness *et al.* 2008). During the evolution of the Rhine River system and its predecessors, the course of the river and its channel types changed through a complex interplay of tectonic processes and climatic influences (Preusser 2008). Information on this evolution is archived in the sedimentary successions. In this study, we examine drill core material from three locations within the Heidelberg Basin. The coring sites correspond to the centre of subsidence of the basin (Heidelberg), the western margin (Ludwigshafen) and the geographic centre of the basin (Viernheim). Each core contains four lithostratigraphic units (Fig. 1), which are described below.

The lowermost Iffezheim Formation (IFm) was deposited during the Pliocene. The sediments were supplied by the adjacent Variscan massifs; thus, the heavy mineral assemblage is dominated by zir-

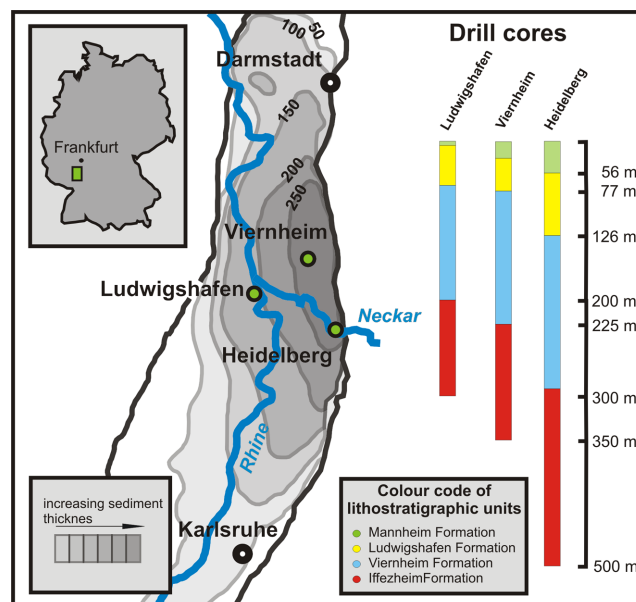


**Figure 1.** Simplified map of the northern Upper Rhine Graben, including information on the thickness of the Quaternary sedimentary fill and the location of the coring sites (green dots; redrawn after Bartz 1974). Inset map shows the location of the basin in Germany (green square). The bars on the right-hand side of the figure illustrate the lengths of the cores and the relative proportions of the respective lithostratigraphic units.

con, rutile-anatase, and tourmaline (Hagedorn & Boenigk 2008; Hoselmann 2008). The mottled reddish, orange and light grey colours of these rocks indicate oxidized fluvial floodplain deposits that were primarily deposited under reducing conditions (Bown & Kraus 1987; Kraus 1999, 2002). The presence of pisolites and root beds is consistent with pedogenesis in a subtropical climate that experienced pronounced summer droughts. A sudden increase in unstable heavy minerals (garnet, epidote and hornblende) accompanied by calcareous material and frequently coarser sediments is attributed to the connection of the Alpine drainage system to the Rhine (Hagedorn 2004; Hagedorn & Boenigk 2008; Preusser 2008). The onset of this alpine mineral suite marks the lower boundary of the overlying lithostratigraphic formation, the Viernheim Formation (VFm; Hoselmann *et al.* 2010). The change in the heavy mineral assemblage was established by Bartz (1959, 1976) and Bartz *et al.* (1982) as representing the Plio-Pleistocene boundary. However, it was clarified by recent work of Scheidt *et al.* (2015) that the magnetic polarity change from the normal Gauss chron to the reversed Matuyama chron occurred prior to the connection of the Alpine drainage system at the top of the IFm. The pelitic strata of the IFm continue into the overlying VFm. Gradually increasing proportions of intercalated greyish fluvial sands, followed by beige and light to dark grey silts and sands, suggest a change in the hydrological regime. After the transition, a persistent high water table prevented the diagenesis and pedogenesis that would have occurred under oxidizing conditions (Rolf *et al.* 2008). The third unit, the Ludwigshafen Formation (LFm), also consists mainly of silts and sands, as well as thin layers of peat. The Mannheim Formation (MFm), which is the uppermost unit, is composed partly of massive sequences of sand to coarse-grained gravel (Hoselmann 2008; Weidenfeller & Knipping 2008; Przyrowski & Schäfer 2015). A detailed description and exact definition of the lithostratigraphic units is given in the German Litholex (Hoselmann *et al.* 2010; Weidenfeller *et al.* 2010; Ellwanger *et al.* 2010a,b). It should be

noted that local conditions cause variations in the lithostratigraphic units between different sites. While the Viernheim and P36 cores are macroscopically similar, the influence of the Neckar alluvial fan produced prominent features in the Heidelberg core. Within the Quaternary part of the core, these include coarser grain sizes, different mineral compositions, and horizons dominated by reddish sediments that are derived from nearby outcrops of Lower Triassic sandstone (Simon 2012).

A sedimentological description of the Viernheim and Heidelberg cores can be found in Hoselmann (2008) and Ellwanger & Wieland-Schuster (2012), respectively, whereas a sedimentological microanalysis of the Mannheim Formation of the Heidelberg core has been published by Menzies & Ellwanger (2015). A detailed description of the Ludwigshafen Parkinsel P36 core is still lacking. Information on the sister cores P34 and P35 is available in Hagedorn (2004); Hagedorn & Boenigk (2008); Wedel (2008), Weidenfeller & Knipping (2008) and Westerhoff *et al.* (2008). General information on the sedimentary source areas of the (Palaeo-)Rhine is provided by Reiter *et al.* (2015) and Tatzel *et al.* (2015). The recently published depositional model of the northern Upper Rhine Graben by Przyrowski & Schäfer (2015) provides a fluvial facies model that shows the sedimentological composition and the fluvial cyclicality of the sediments of the Heidelberg Basin. However, their ‘geohistory curve’ is not consistent with the established magnetostratigraphy (Scheidt *et al.* 2015).

### 2.1 The Viernheim drill core

The site of the Viernheim drill core, which was obtained in 2006, is located in the Hessian Ried (Buchner-Schneise), approximately 3 km north of the city of Viernheim (N 49.565916 E 8.571516 (WGS84)). The core is enclosed in liners over its entire length of 350 m. The liners and cores were cut into 1 m pieces, which were subsequently bisected. The working halves were stored unwrapped to enable natural desiccation. Cubic specimens with a volume of  $\sim 10 \text{ cm}^3$  were collected at  $\sim 50 \text{ cm}$  intervals. Interesting sections identified by visual inspection were sampled at a closer spacing. Sections consisting of medium-grained sand were sampled by cutting cylindrical samples with a diameter of 2.54 cm (1 inch) perpendicular to the core axis. Coarse sandy and gravelly sections were generally not sampled. Additional core material was taken for magnetic extractions (Section 2.4) at  $\sim 10 \text{ m}$  intervals.

### 2.2 The Heidelberg drill core

The Heidelberg site includes two cores collected from sites that are close to one another in the city of Heidelberg. The first drilling project (UniNord 1) stopped at a depth of  $\sim 190 \text{ m}$  in 2006 (N 49.424992 E 8.663045 (WGS84)). A second drill core (UniNord 2), which is located  $\sim 260 \text{ m}$  from the first core, was obtained in 2008 (N 49.427255 E 8.662037 (WGS84)). During the second drilling project, core material was retrieved between 113 and 114 m and from 184 m to the final depth of 500 m. The congruity of the two Heidelberg drill cores was demonstrated by the negligible ( $\sim 1 \text{ m}$ ) offset between corresponding magnetostratigraphic signatures related to the Jaramillo subchron (Scheidt *et al.* 2015). Therefore, it was possible to merge the data obtained from the two cores into a composite record with a total length of 500 m.

Sampling of the Heidelberg cores, which were also enclosed in liners, was performed as described in Section 2.1, including additional material for magnetic extractions.

### 2.3 The Ludwigshafen drill core

Several drill cores are available from groundwater exploration boreholes in the city of Ludwigshafen (N 49.469115 E 8.461574 (WGS84)). We focus on core P36, which reached a final depth of 301 m in 2009. Like the other cores, P36 was entirely enclosed in liners. The dried working half of the bisected core was sampled at 0.5 m intervals in 2012 by cutting cubic samples as described in Section 2.1. Additional material was collected every  $\sim 10 \text{ m}$  for magnetic extraction.

### 2.4 Magnetic extraction procedure

Core material for the selective extraction of magnetic minerals was gently crushed with a mortar and pestle and subsequently sieved with a 500  $\mu\text{m}$  mesh. 50 g of the  $< 500 \mu\text{m}$  fraction were used for magnetic extraction. For this purpose, sieved material was disaggregated using ultrasonic treatment and subsequently loaded into a magnetic extraction apparatus (Petersen *et al.* 1986). The speed of the peristaltic pump was regulated according to the grain size of the material. To inhibit clogging, we set the speed to 50–80 rpm for sands and 30–50 rpm for silts. The extracted minerals were stored in pure ethanol to prevent oxidation processes. The extraction procedure was continued until no more mineral grains were attracted by the magnet finger. A full cycle was usually completed in  $\sim 12 \text{ hr}$ . The extracted material was poured into a beaker with a magnet fixed at the bottom and cleaned by repeated rinsing with demineralized water and ultrasonic treatment. Finally, the solid phase was magnetically separated from the liquid phase and dried on a hot plate at  $\sim 30^\circ\text{C}$ .

### 2.5 Samples for the vibrating sample magnetometer (VSM)

VSM samples were prepared only from sediments hardened in the course of drying, not from loose sediments. For this purpose, samples with an edge length of  $\sim 5 \text{ mm}$  were cut. Only irregularly shaped samples could be obtained in this manner, due the brittle nature of the sedimentary material; thus, their volumes could not be determined.

Samples of magnetically extracted material were prepared by dispersing the extract in a drop of diamagnetic cement.

## 3 MEASUREMENT PROCEDURES

Magnetic measurements were performed in the Grubenhagen palaeomagnetic laboratory of the Leibniz Institute for Applied Geophysics, unless otherwise specified. Different equipment was used, as specified below.

A Magnon VFSM Susceptibility Bridge was used to measure low-frequency magnetic susceptibility ( $\chi_{\text{lf}}$ ) and high-frequency magnetic susceptibility ( $\chi_{\text{hfr}}$ ); the measurements were performed at 505 Hz and 5005 Hz, respectively. Natural remanent magnetization (NRM), IRM and backfield IRM demagnetization curves were measured with a 2G-760SRM-RF-SQUID three-axis cryogenic magnetometer (here abbreviated as 2G-CM; Rolf 2000). If the intensity of the remanent magnetization exceeded the measurement range of the 2G-CM ( $10 \text{ A m}^{-1}$ ) a Magnon Spinner Magnetometer was used instead. IRMs and backfield IRMs were produced with a Magnon PM II Pulse Magnetizer.

The IRM acquisition curves were acquired in 16–20 logarithmically spaced steps up to a maximum field of 2.7 T. The magnetization

acquired at 2.7 T is considered here to represent the saturation remanence (SIRM), even in cases where the high-coercive mineral components were not completely saturated in this field. The coercivity of remanence ( $B_{cr}$ ) was determined from backfield demagnetization curves of SIRM in fields up to at least 300 mT. More detailed IRM acquisition and backfield demagnetization curves were measured with a MicroSense EZ7 vibrating sample magnetometer (VSM) in 49–100 logarithmically distributed steps up to 1.4 or 1.8 T. This instrument was also used to measure magnetic hysteresis loops in a maximum field of 1.4 T, or 1.8 T for samples containing high-coercivity minerals. Strong-field (1 T) thermomagnetic curves  $M_r(T)$  were measured with the same instrument in air between 30 and 700 °C with heating/cooling rates of 30 and 50 °C min<sup>-1</sup>, respectively.

Hysteresis loops and IRM acquisition curves of 20 samples were measured with an EV9 VSM Vibrating Sample Magnetometer at the rock magnetic laboratory of the Institute of Geophysics, Academy of Sciences of the Czech Republic in Prague. The hysteresis parameters  $M_{rs}$ ,  $M_s$ ,  $B_{cr}$  and  $B_c$  were determined with the EasyVSM software by MicroSense.

The magnetic extracts from the P36 core were analysed by SEM (backscattered electrons; FEI Sirion 200, Type D1625) combined with EDX (Ametek, Genesis 4000) for determination of chemical compositions. For this purpose, small amounts of the extracts were placed on carbon-tape-equipped sample holders. No coating technique was applied. The relative detection limits of EDX are within 0.1 wt% for the main elements that are our focus. These analyses were performed in the laboratory of the Federal Institute for Geosciences and Natural Resources (BGR) (Hannover, Germany).

High-resolution first-order reversal curves (FORCs; Pike *et al.* 1999; Roberts *et al.* 2000) were measured at room temperature with a Princeton Measurements Alternating Gradient Magnetometer AGM (Model MicroMag 2900) at the Faculty 5 Geosciences, University of Bremen (Germany). Because of the long time required for a single FORC measurement (5–6 hrs) and the need to perform 6–9 repeated measurements on weak specimens, only a few samples could be characterized with this technique. Suitable samples were selected according to their hysteresis properties and after preliminary low-resolution measurements, which were performed to ensure coverage of all types of FORC signatures encountered in the three cores. FORC measurement protocols were selected according to Egli *et al.* (2010) and extended to higher fields, if necessary, while maintaining field steps below 1 mT for the detection of high-resolution signatures (Table 1). FORC measurement processing and plotting was performed with the VARIFORC software package (Egli 2013). This software package enables the processing of multiple measurements from the same specimen for the improve-

ment of weak signals, as well as the use of an optimized smoothing protocol for the correct representation of high-resolution features such as the central ridge and background contributions with very low signal-to-noise ratios.

The individual coercivity components were identified via coercivity analyses of the IRM acquisition curves using the Mag-Mix coercivity analysis software package (Egli 2003, 2004a). The software utilizes skewed generalized Gaussian (SGG) curves (Egli 2003, 2004b), which are based on cumulative log Gaussian (CLG) curves and include later improvements (Robertson & France 1994; Stockhausen 1998; Kruijver *et al.* 2001; Heslop *et al.* 2002; Leonhardt 2006; Heslop & Dillon 2007). Performing a coercivity analysis with Mag-Mix is a two-stage procedure. First, the coercivity distributions on a logarithmic field scale are calculated from magnetization curves (Egli 2003). All coercivity distributions are then modelled with a linear combination of a given number  $m$  of identical SGG functions. That is, for the  $k$ th specimen,

$$f_k(\log H) = \sum_{i=1}^m M_{ki} \text{SGG}(\log H, \mu_i, \sigma_i, s_i, 2), \quad (1)$$

where  $M_{ki}$  is the total remanent magnetization of the  $i$ th coercivity component in the  $k$ th specimen,  $\mu = \log_{10} B_{1/2}$ , and  $B_{1/2}$  represents the median acquisition field. Furthermore, the dispersion parameter  $\sigma$  (referred to as DP in case of CLG functions) corresponds roughly to the logarithmic standard deviation of the coercivity distribution, the asymmetry of the coercivity distribution on a logarithmic scale is controlled by the skewness parameter  $s$ , and the squareness of the function is described by the squareness parameter  $p$ . This latter parameter is set in nearly all cases to  $p = 2$  (corresponding to the squareness of a Gaussian function), as this appears to be the natural value of most magnetic components (Egli 2004b).

To avoid incorrect estimations of the number of components present, the multi-specimen analysis function in the Mag-Mix software package was applied. Notice that all of the components are characterized by the same shape parameters  $\mu_i$ ,  $\sigma_i$ , and  $s_i$ , so this analysis is suited only to groups of samples containing the same magnetic components in different proportions. The parameters  $\mu_i$ ,  $\sigma_i$  and  $s_i$  are determined by minimizing the root mean square of all model residuals. The main advantage of this procedure over the analysis of individual curves is that the solutions are stabilized, eliminating the well-known instability problems arising from the flexible shape of SGG functions (Egli 2003, 2004a).

A total of 507 IRM acquisition curves measured with the 2G-CM were analysed with Mag-Mix. To handle this large number of samples, coercivity distributions taken from step one of the Mag-Mix processing were grouped into sets with similar curve shapes.

**Table 1.** List of samples analysed using FORC measurements.

Name	Lithol.	T-group	Number of runs	$H_c$ min/max [mT]	$H_b$ min/max [mT]	B sat [mT]	Pauses	Average time	Anzahl FORCs (N)	Field increment [mT]
P104-37	VFm	C	8	0/120	-40/60	300	0.5 s	0.1 s	450	0.515
UN036-33	MFm	A	6	0/120	-40/60	300	0.5 s	0.1 s	450	0.515
			6	0/800	-80/150	1030	0.5 s	0.1 s	450	2.37
UN080-22	LFm	C	6	0/160	-40/90	300	0.5 s	0.1 s	450	0.667
UN458-96	IFm	A	6	0/120	-40/90	300	0.5 s	0.1 s	450	0.515
			6	0/600	-40/80	800	0.5 s	0.1 s	400	1.87
V043-28	LFm	C	8	0/120	-40/60	300	0.5 s	0.1 s	450	0.515
V194-17	VFm	A	6	0/140	-50/70	300	0.5 s	0.1 s	550	0.5
V213-87	Vfm	A	9	0/120	-40/60	300	0.5 s	0.1 s	450	0.515

*Note:* Besides the FORC parameters, the respective lithostratigraphic units of the samples and their thermomagnetic group affiliations used in Section 4.2 are indicated.

Combined modelling was then applied to the members of each group. The combinations of components that were used to model groups of samples are called 'clusters' in this work. Samples that could not be modelled sufficiently within their initially assigned group were processed separately. In most cases, components of other clusters could be used.

## 4 RESULTS AND INTERPRETATION

In the present study, a major obstacle to systematic analysis arises from the use of large amounts of bulk sample material that is extremely heterogeneous in composition, texture, and grain size spectra. For example, most bulk magnetic parameters do not support a clear sample classification, while detailed characterizations, such as coercivity analysis and FORC, were necessarily limited to a very small number of samples. In the following, we report on the principal findings obtained with the techniques mentioned in Section 3.

### 4.1 EDX/SEM

A combined EDX and SEM analysis was performed for 238 grains from 25 magnetic extracts of samples from P36 core. The information received on the mineralogy and chemical composition of these grains was used to gain a better understanding of the origin and the diagenetic history of the minerals. Sediments of the MFm were too coarse to be processed by our magnetic extraction apparatus. Hence, the particles examined were only obtained from the LFm (48 pc.), the VFm (101 pc.) and the IFm (89 pc.). The limited number of investigated grains does not allow for systematic interpretation of down-core trends. Nevertheless, useful information on characteristic compositions and structures was obtained.

Magnetic minerals were identified by combining visual characteristics (grain shape, surface appearance and texture) with EDX-derived elemental abundances, whereby submicron intergrowths or subsolidus exsolution textures may lead to inconclusive results.

Examination of 238 grains revealed the dominance of iron-titanium minerals (61.3%), including magnetite, maghemite, and haematite (Fig. 2). The majority of these minerals occurs as detrital particles or microcrystalline aggregates. Idiomorphic crystals and authigenic formations appear only very occasionally. Some

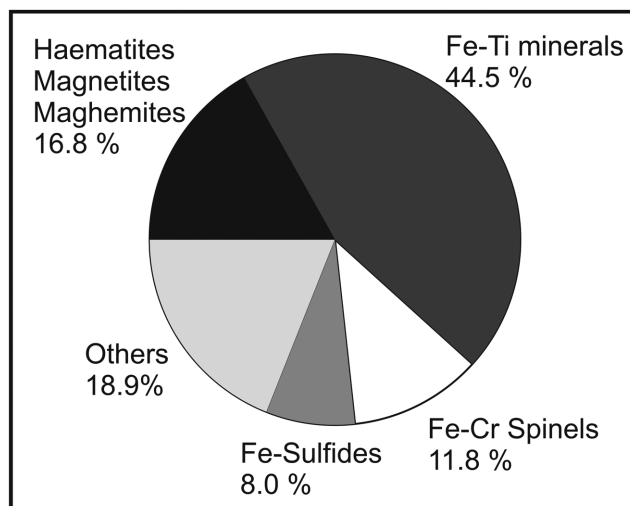


**Figure 2.** Pie chart of minerals identified by EDX analysis. The percentages refer to the total number of 238 analysed grains.

particles show shrinkage cracks, which typically occur during low-temperature oxidation of magnetite to maghemite (Petersen & Vali 1987; Gapeev & Tsel'movich (1988) in Dunlop & Özdemir (1997)) or during leaching of Fe from ilmenite (Khor *et al.* 1996; Ahmed *et al.* 2010). The presence of effectively paramagnetic ilmenite in magnetic extracts can be explained by the presence of Fe-enriched micro-structural twin-domains (Lawson & Nord 1984; Nord & Lawson 1989), ferrimagnetic substructures (McEnroe *et al.* 2002) or ferrimagnetic inclusions. Since particles that have similar chemical compositions but show dissolution features to different extents (Fig. 3b) can be found within the same sample, different diagenetic histories are assumed. We propose that detrital minerals with the least alteration are representative of the in situ diagenesis that has taken place within particular stratigraphic levels, with variations arising from individual burial-erosion cycles. Since physical abrasion during transport would have been destructive, the amount of in situ dissolution is likewise indicated by the fragile trellis-like habits of titanomagnetite grains showing the oxyexsolution intergrowth texture inherited from the high-temperature portion of their history (Price 1980; Tucker & O'Reilly 1980; Gapeev & Tsel'movich (1983) in Dunlop & Özdemir (1997).

Detrital iron-chromite spinels are the second most common mineral group (11.8%) in the magnetic extracts. Chromite is only magnetically extractable if the magnetite component exceeds 40% (Hounslow 1996). We distinguish three main mineral groups according to their Ti/Fe and Cr/Fe element ratios (Fig. 4):

- (1) Titanium-free crystals from the magnetite ( $\text{Fe}_3\text{O}_4$ )–chromite ( $\text{FeCr}_2\text{O}_4$ ) solid solution series plot along the  $\text{Ti/Fe} = 0$  line in Fig. 4(a).
- (2) Ti-substituted chromites are grouped on the right-hand side of Fig. 4(a).
- (3) The third group, which has scattered element ratios, includes Cr-containing Fe-Ti minerals with Ti/Fe ratios between 0.024 and 1.3.

Consistent with the results of Hounslow (1996), the extent of corrosion of chromite grains increases with higher Fe content. The small amounts of manganese (mean: 0.92%, max 6%) detected in most chromites may have significant effects on their magnetic properties (Hounslow 1996).

Iron sulphides are another important magnetic mineral group (8%). In spite of their relative low abundance (Fig. 2), four different morphologies were noted. The majority of all iron sulphides occurs as microcrystalline aggregates, which generally adhere to grain surfaces, when they are very small. A small number of pseudo-morphic mineral fragments and tiny euhedral crystals were also found, along with a few framboidal aggregates (Figs 3a and c). Perfectly round framboids (Fig. 3a) are generally composed of pyrite or greigite (Wilkin & Barnes 1997). Two distinct grain size groups can be distinguished in the framboid shown in Fig. 3(a). Roberts & Weaver (2005) and Roberts (2015) described similar masses of euhedral Fe-sulphides, in which the finest-grained crystals are made up of greigite, whereas the coarser ones are made up of pyrite. Due to their small size ( $\sim 1 \mu\text{m}$ ) and compact arrangement, the compositions of the individual crystals cannot be identified unambiguously with EDX spectra. However, because of their occurrence in the magnetic extracts, we suggest that these aggregates are composed mainly of ferrimagnetic greigite.

Finally, almost 19% of the analysed particles fall into other categories (Fig. 2), which collectively include non-magnetic minerals (e.g. iron carbonates, detrital zircons, and amphiboles) and

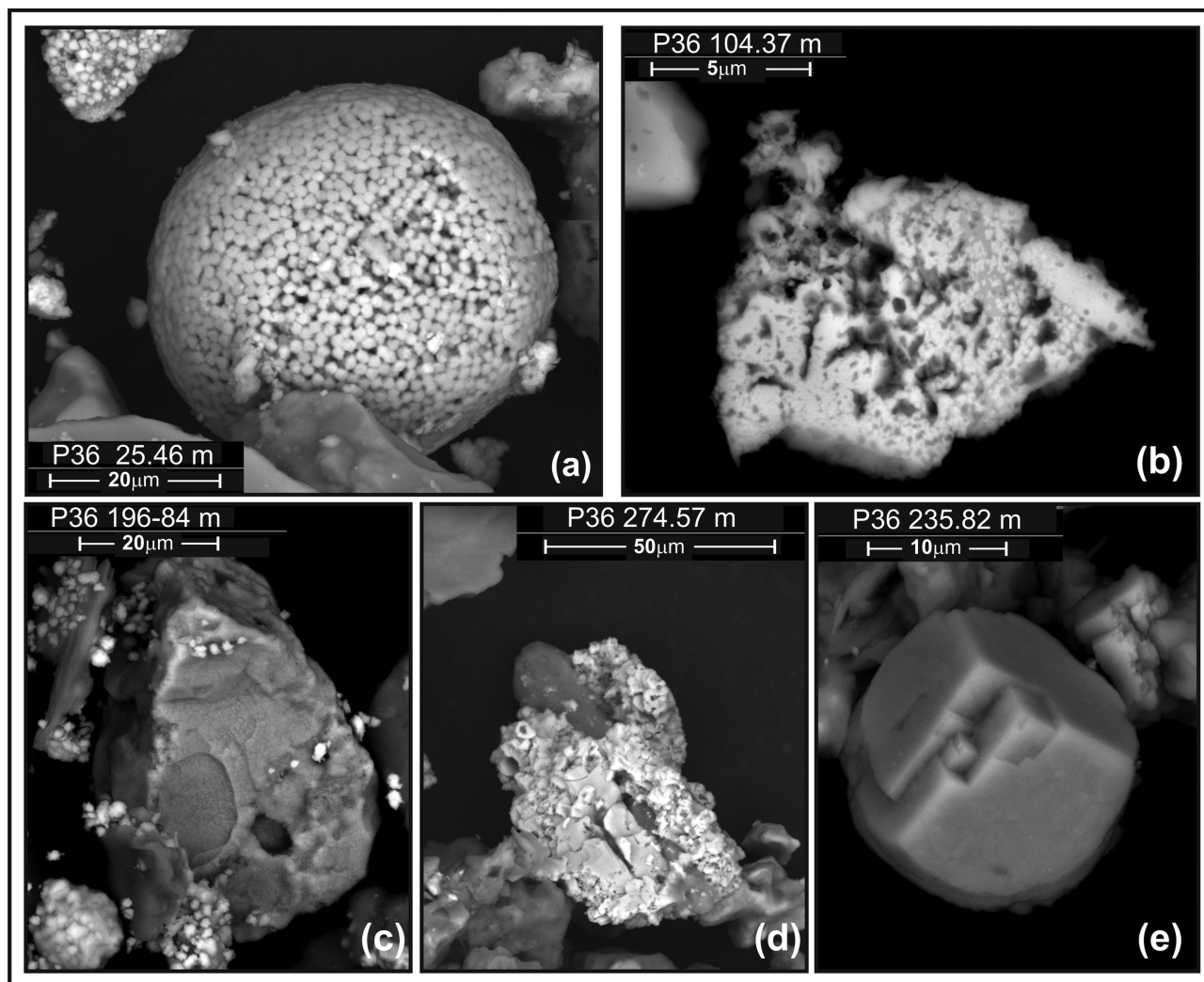


**Figure 3.** SEM images of non-coated minerals from core P36. (a) Framboidal sulphide mineral (most likely greigite) and an irregular aggregate of sulphides consisting of larger single crystals and much smaller fine crystalline minerals (greigite, pyrite?). (b) Porous remainder of a Fe-Ti mineral; iron depletion causes the spotted appearance. (c) Ilmenite showing microcracks on the surface and surrounded by flaky sulphide minerals. (d) Quartz grain overgrown with specularite. (e) Pseudo-morph of haematite after pyrite.

unidentifiable minerals with inconclusive elemental compositions, as well as polymineralic microcrystalline aggregates.

Magnetic extracts from all stratigraphic levels contain a significant amount of silicates and aluminosilicates. Backscatter micrographs show tiny ( $\leq 1 \mu\text{m}$ ), bright minerals covering some of these grains that may have caused their extraction. Paramagnetic minerals without ferrimagnetic properties that adhere to the surface are suspected to have been extracted due to ferrimagnetic inclusions.

In conclusion, the magnetic mineral assemblages of the three lithostratigraphic units, the IFm, the VFm, and the LFm, are characterized by the following main elements:

(1) The occurrence of strongly corroded magnetite remnants (similar to Fig. 3b) is restricted to the VFm and the LFm, whereas haematite (specularite) was exclusively identified in extracts from the IFm (Fig. 3e). It should be noted that the slightly pitted surfaces of some haematite particles indicate the action of iron dissolution processes after the formation and deposition of these grains.

(2) Apart from two outliers, these lithostratigraphic units yield maximum Ti/Fe ratios (Fig. 5) of 1.4, 1.8 and 4 for the LFm, the VFm and the IFm, respectively. This trend can be interpreted in

terms of the different origins of the minerals, as well as by changes in diagenetic conditions. A change in the sediment provenance of the Rhine River was caused by the connection of the Alpine Rhine and the Aare/Rhine system in the late Pliocene and is characterized by the appearance of an admixture of unstable heavy minerals (Hagedorn 2004; Hagedorn & Boenigk 2008; Hoselmann 2008). Although parts of the Quaternary deposits originated continuously from the margins of the Upper Rhine Graben and occasionally even dominate the sequence within distinctive intervals (Hagedorn & Boenigk 2008), Ti/Fe-ratios comparable to those of the IFm were not found in the VFm and the LFm (Fig. 5). The magnetic minerals of the IFm are thus more influenced by iron leaching and relative enrichment in Ti and Cr, which is a typical feature of reworked and diagenetically overprinted sediments (Dimanche & Bartholome 1976; Roberts & Turner 1993; Hounslow *et al.* 1995, 1996; Khor *et al.* 1996; Wilson & Roberts 1999; Nowaczyk 2011; Roberts 2015). According to a number of authors (e.g. van Houten 1968; Dimanche & Bartholome 1976; Maher & Hallam 2005), the chemical alteration of magnetite and ilmenite occurs after deposition, rather than during the first stages of erosion and fluvial transport. Consequently, the higher Ti/Fe-ratios of the IFm are caused by a formation history that

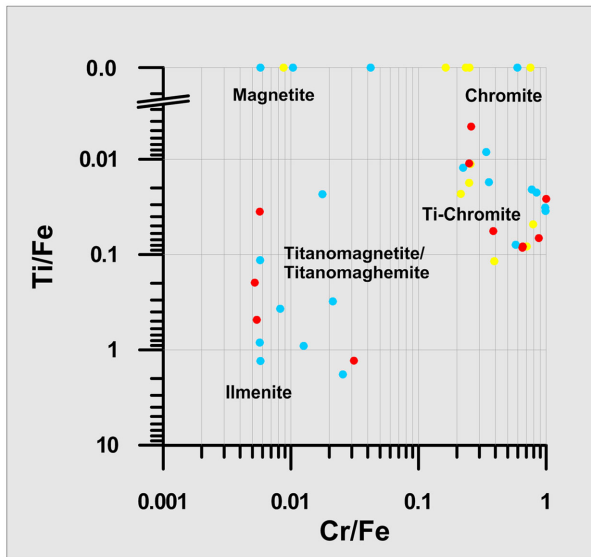


**Figure 4.** Element ratios of Cr and Ti containing magnetic minerals extracted from core P36 measured by EDX analysis (based on atomic percentages). Unit colour code follows that used in Fig. 1: yellow, LFm; blue, VFm; red, IFm.

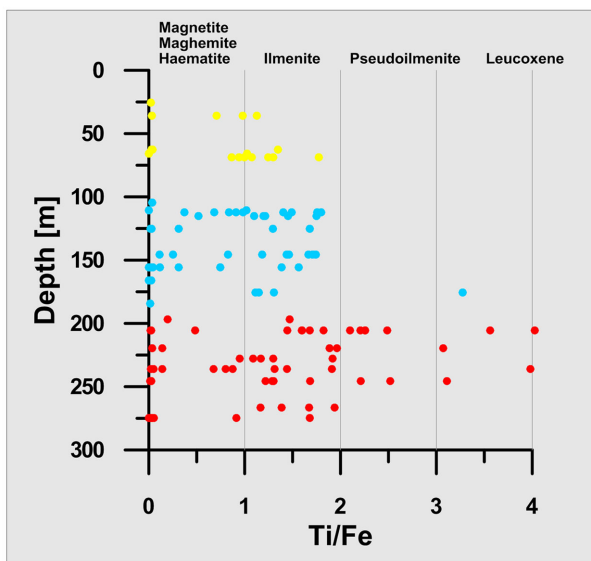


**Figure 5.** Ti/Fe ratios of iron–titanium minerals of extracts from core P36 as a function of depth. Unit colour code follows that used in Fig. 1: yellow, LFm; blue, VFm; red, IFm.

differs from that of the LFm and the VFm. For the same reasons, differences in diagenetic conditions can be assumed, including various biological, physical, and chemical processes that may affect magnetic mineral associations.

(3) Fe-sulphides are relatively abundant down to a depth of 196.80 m (the top of the IFm), whereas only two sulphide grains and a few traces of sulphur were found in the strata below. The identification of an iron oxide pseudo-morph after pyrite at a depth of 274.57 m shows that pyrite formed authigenically and was diagenetically replaced at a later stage (Fig. 3e). Thus, Fe-sulphides were originally more abundantly represented in the IFm.

## 4.2 Thermomagnetic analyses

The temperature dependence of ‘saturation’ magnetization in a strong magnetic field provides diagnostic information about the composition of ferrimagnetic minerals through their Curie or Néel temperatures, as well as the characteristic alteration temperatures at which magnetic minerals decompose or new magnetic minerals form. Because of the complex set of chemical reactions that occur in sediment upon heating, thermomagnetic analyses are limited to magnetic extracts, which significantly reduces the possible complications related to the alteration of non-magnetic minerals. For comparison, all curves are normalized by their initial magnetization (Fig. 6).

All thermomagnetic curves can be divided into the following three main groups:

(A) Type A contains heating curves that are characterized by monotonic decreases until full disappearance of magnetization between 600 and 700 °C, which is the typical Curie temperature range of pure iron oxides (i.e. magnetite, maghemite, and haematite). Some curves show an enhanced loss of magnetization between 450 and 630 °C.

(B) These curves are similar to type A up to 400 °C, but a marked magnetization increase that peaks between 400 and 450 °C occurs subsequently. In some cases, a main peak is followed by a secondary peak (Fig. 6c). A rapid magnetization loss occurs above 550 °C. Type B samples are exclusively found in the IFm.

(C) Multiple irregular peaks with relatively prominent increases between 250 and 290 °C characterize C-type heating curves. Two main groups of peaks are identifiable; the first occurs around ~300 °C and the second is found at approximately 500 °C. Flat or slightly inclined sections may replace either or both peaks. Only two samples from the IFm fall into group C.

Thermal alteration processes are indicated by irreversible behaviour in all heating experiments. The cooling curves start to increase between 620 and 580 °C and have generally similar curved shapes. When little evidence for re-crystallization processes and new mineral formations is shown by the heating curves, cooling curves fall below the heating curves (type A and some type C), and suggests the conversion of magnetic minerals into less magnetic ones (e.g. by the oxidation of magnetite into haematite). In the case of heating curves that reflect strong alteration (groups B and C), the magnetization at the end of the heating-cooling cycle exceeds the initial one by up to a factor of 20, implying that weakly magnetic or non-magnetic minerals have been converted into strongly magnetic minerals (e.g. by the oxidation of pyrite into magnetite).

Type-A thermomagnetic curves are typical of relatively stable mineral assemblages containing magnetite, maghemite and/or haematite (e.g. Özdemir 1990; de Boer & Dekkers 1996; Liu *et al.* 2010). Curie temperatures below that of the pure magnetite end-member most likely occur due to the substitution of Fe by Cr and Ti (Schmidbauer 1969; Gendler *et al.* 1979; Murthy & Krishnamacharyulu 1994; Maksimochkin *et al.* 2013) or aluminium (Da Costa *et al.* 1995; de Boer & Dekkers 1996). Curie temperatures exceeding that of the magnetite end-member can originate from impurities in the crystal lattice, exsolution fabrics or partial or complete oxidation to maghemite ( $T_C \sim 640^\circ\text{C}$ ) or haematite ( $T_N \sim 680^\circ\text{C}$ ) (e.g. Schmidbauer 1969; Price 1980; de Boer *et al.* 2001; Liu *et al.* 2010). Natural maghemite is also known to contain imperfections and internal stresses, which decrease its Curie temperature.

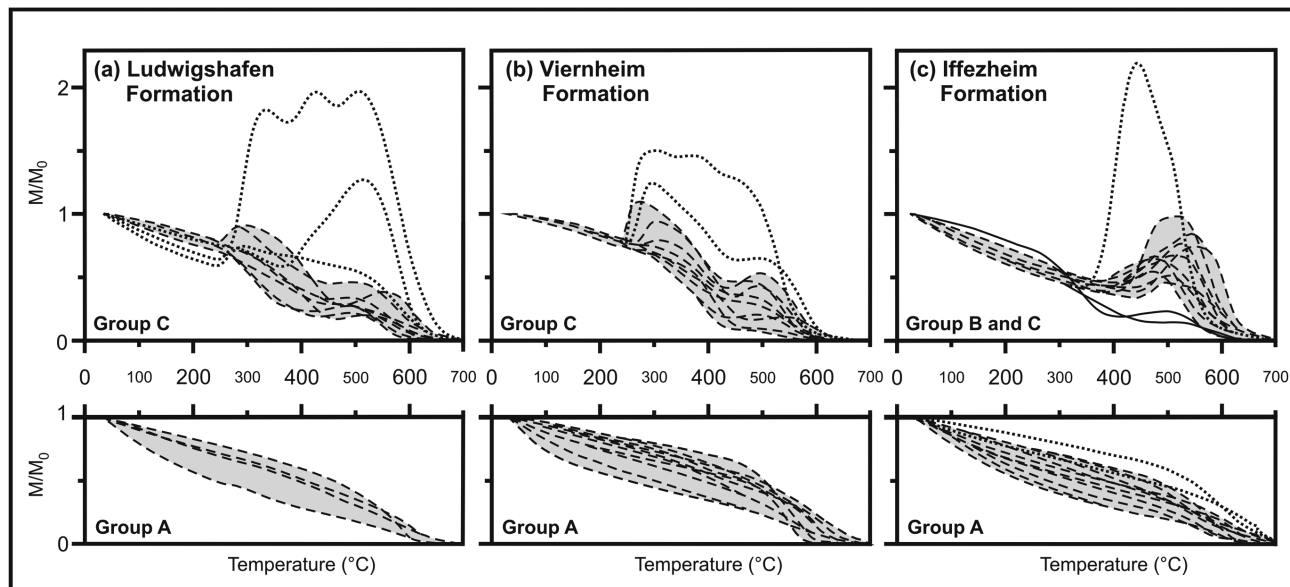


**Figure 6.** Thermomagnetic measurements of samples from different lithostratigraphic units divided into groups A, B and C. Shaded areas confine regions in which the heating curves run across. Exemplary pathways are depicted using dashed lines. Outliers are shown with dotted lines. The continuous lines in (c) represent type-C specimens. For detailed explanations, see the text.

In addition to the abovementioned phases, minerals within the ferrimagnetic range of the haematite-ilmenite solid solution series were identified in SEM/EDX analyses of group-A samples from the IFm. These minerals are characterized by a linear dependence of the Curie temperature on the degree of Fe substitution, and these Curie temperatures range from  $-218^{\circ}\text{C}$  for the ilmenite end-member to  $680^{\circ}\text{C}$  for the haematite end-member, respectively (Reynolds 1977). We assume that ferrian ilmenites carry only a small part of the sediment magnetization, which is not detected by thermomagnetic measurements.

The magnetization peak that occurs at approximately  $500^{\circ}\text{C}$  for group B samples can be attributed to the conversion of thermally unstable minerals to a new magnetic phase. A strong candidate for this signature is pyrite, which starts to decompose at  $400\text{--}500^{\circ}\text{C}$ , giving rise to a magnetization increase at approximately  $500^{\circ}\text{C}$  (Passier *et al.* 2001; Weaver *et al.* 2002; Hu *et al.* 2006). Paramagnetic pyrite may occur in the extracts due to intergrowth or aggregation with any ferrimagnetic minerals that are present. Alternatively, incomplete decomposition may lead to a pyrite core with an oxidized rim. Other possible but less likely candidates for the magnetization peak seen in group B are natural chromites (Kumar & Bhalla 1984) and siderite (Housen *et al.* 1996; Pan *et al.* 2000). The temperature range of the final magnetization loss is indicative of the formation of impure magnetite.

Group C is characterized by the most complex thermomagnetic behaviour. The blocking temperatures are consistent with a wide range of magnetic minerals. Although some type-C specimens can be explained by multiple conversions of only one primary phase, they are more likely to reflect multicomponent mixtures with varying proportions of the minerals involved. Possible candidates are solid solutions of the paramagnetic chromite ( $\text{FeCr}_2\text{O}_4$ ) and magnetite ( $\text{Fe}_3\text{O}_4$ ) end-members. In this case, the corresponding Curie temperatures range from  $0$  to  $580^{\circ}\text{C}$  (Schmidbauer 1969; Schmidbauer 1971; Hounslow *et al.* 1995). Some natural chromites are reported to be characterized by two phases, one of which has a blocking temperature between  $300$  and  $350^{\circ}\text{C}$  (which is attributed to chromite), and an associated magnetite phase with a blocking temperature between  $550$  and  $600^{\circ}\text{C}$  (Murthy & Krishnamacharyulu

1994; Hounslow 1996; Kądziałko-Hofmokr *et al.* 2010). The oxidation of thermally instable maghemite to haematite can also lead to a progressive magnetization loss starting from  $250^{\circ}\text{C}$  (Verwey 1935; Bernal *et al.* 1957).

The first peak at  $250\text{--}270^{\circ}\text{C}$  can be attributed to the structural transition of fine-grained pyrrhotite (Schwarz & Vaughan 1972; Dekkers 1989), whereas the second peak at  $500^{\circ}\text{C}$  is attributable to the decomposition of sulphidic components. As discussed for group B specimens, pyrite is a possible contributor, along with greigite, which was previously detected in the VFm and the LFM in former studies (Rolf *et al.* 2008; Scheidt *et al.* 2015). Greigite is characterized by a moderate magnetization decay up to  $300^{\circ}\text{C}$ , followed by a more pronounced loss. The latter signature is not observed in most of the samples, probably caused by the superposition of contributions from other minerals. After decomposition at  $\sim 340^{\circ}\text{C}$ , a peak in intensity approximately  $500^{\circ}\text{C}$  is due to the neo-formation of magnetite (Roberts 1995; Roberts *et al.* 2011).

Group C outliers are characterized by a marked magnetization plateau between  $300$  and  $500^{\circ}\text{C}$  that is due to the occurrence of several peaks caused by different magnetic phases that may have formed during heating or were already present in the pristine sample material. Similar signatures are frequently found in natural sediments, and their cause is uncertain. Some similarities exist with curves arising from the reaction chain in which lepidocrocite is converted to maghemite intermediates and finally to haematite. Such conversions are usually characterized by double-peaked demagnetization curves that contain sharp increases at  $\sim 250^{\circ}\text{C}$  and drops between  $430$  and  $480^{\circ}\text{C}$  (Gehring & Hofmeister 1994; Gendler *et al.* 2005). However, multiple peaks are possible if additional magnetic phases are involved. The final demagnetization between  $500$  and  $640^{\circ}\text{C}$  can again be ascribed to the presence of impure magnetite or thermally stable maghemite, as discussed above.

### 4.3 Magnetic susceptibility

The down-core variations in mass-normalized magnetic low-frequency susceptibility ( $\chi_{lf}$ ) are characterized by similar trends

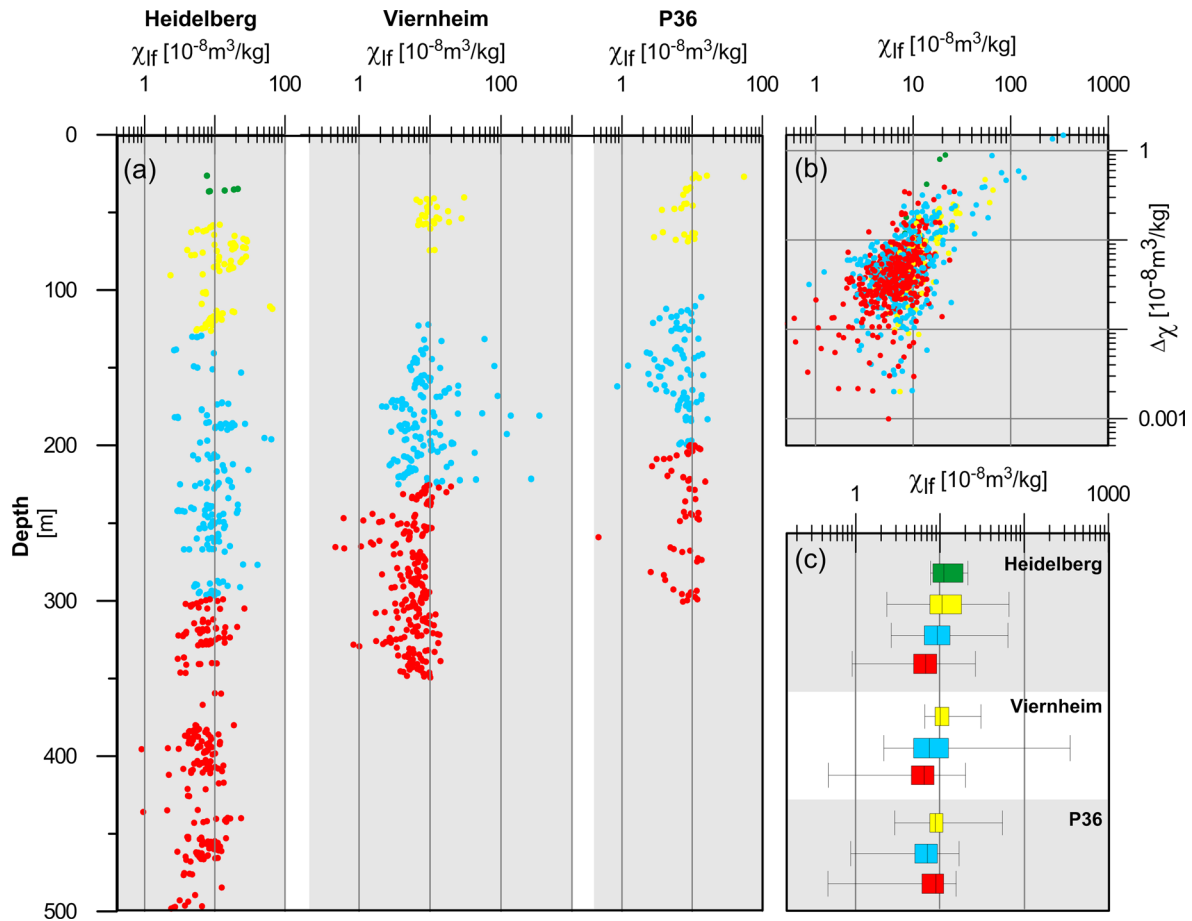


**Figure 7.** (a) Mass-normalized susceptibility ( $\chi_{lf}$ ) versus core depth. (b)  $\chi_{lf}$  versus absolute frequency dependence of susceptibility ( $\Delta\chi$ ) of bulk sample material. Four data points of the VFm within the Viernheim core with  $\chi_{lf} > 100$  and  $\chi_{fd} < 1$  are omitted to permit better visualization of the remaining data. (c) Box-and-whisker plot of susceptibility ranges. (a, b, c) Unit colour code follows that used in Fig. 1: green, MFm; yellow, LFm; blue, VFm; red – IFm.

in all three cores (Fig. 7). Values reach up to  $345 \times 10^{-8} \text{ m}^3 \text{ kg}^{-1}$ , and mean values of the individual formations range between  $7.2$  and  $13.1 \times 10^{-8} \text{ m}^3 \text{ kg}^{-1}$ . Differences between these values and those reported in Scheidt *et al.* (2015) arise from the measurement of a slightly different set of samples and the use of a different measuring device.

As expected, the IFm exhibits relatively low susceptibility values because of the presence of authigenic haematite formed by oxidation of the primary magnetic mineral assemblage. The highest susceptibility values are attributed to the occurrence of ferrimagnetic sulphides or heavy mineral placer in the VFm. Heavy mineral placers have occasionally been recognized by rich yields of coarse magnetic minerals in the magnetic extraction procedure.

The relative frequency dependence of magnetic susceptibility, expressed as  $\chi_{fd} = 100(\chi_{lf} - \chi_{hf})/\chi_{lf}$ , never exceeds 4.3%, and the low average value of 0.63% points to very small contributions from SP particles to the magnetic signal in the majority of the sediments (Table 2).

The absolute frequency dependence of susceptibility,  $\Delta\chi = \chi_{lf} - \chi_{hf}$ , is only roughly correlated with  $\chi_{lf}$  (Fig. 7b). The scatter is the result of domain state and mineralogical variations, which dominate the variations in SP concentration.

Important additional information for the interpretation of frequency dependent susceptibility is gained from the dark grey/black, clayey sample material of the archived Heidelberg half-core by its susceptibility decrease to almost zero upon drying. This loss can be

**Table 2.** Median, minimum and maximum frequency dependent susceptibility  $\chi_{fd}$  of the cores and the respective lithostratigraphic units.

Lith.	<i>N</i>	Median $\chi_{fd}$	Min $\chi_{fd}$	Max $\chi_{fd}$
Heidelberg				
MFm	6	2.59%	0.00%	4.29%
LFm	75	0.62%	0.08%	1.15%
VFm	128	0.66%	0.00%	1.95%
IFm	215	0.71%	0.00%	3.52%
Viernheim				
LFm	25	0.51%	0.21%	1.59%
VFm	134	0.64%	0.00%	2.97%
IFm	204	0.54%	0.00%	4.22%
P36				
LFm	24	0.83%	0.00%	1.55%
VFm	79	0.62%	0.00%	3.70%
IFm	53	0.65%	0.00%	3.64%

Note: Number of measured samples (*N*).

attributed to the oxidation of diagenetic SP sulphide particles that were originally preserved under sealed conditions. In summary, the observed minor frequency dependence of magnetic susceptibility results either from disappearance of SP magnetite/maghemite during oxidizing or reducing diagenesis (Roberts 2015) or from oxidation of SP sulphides during desiccation of the cores and samples.

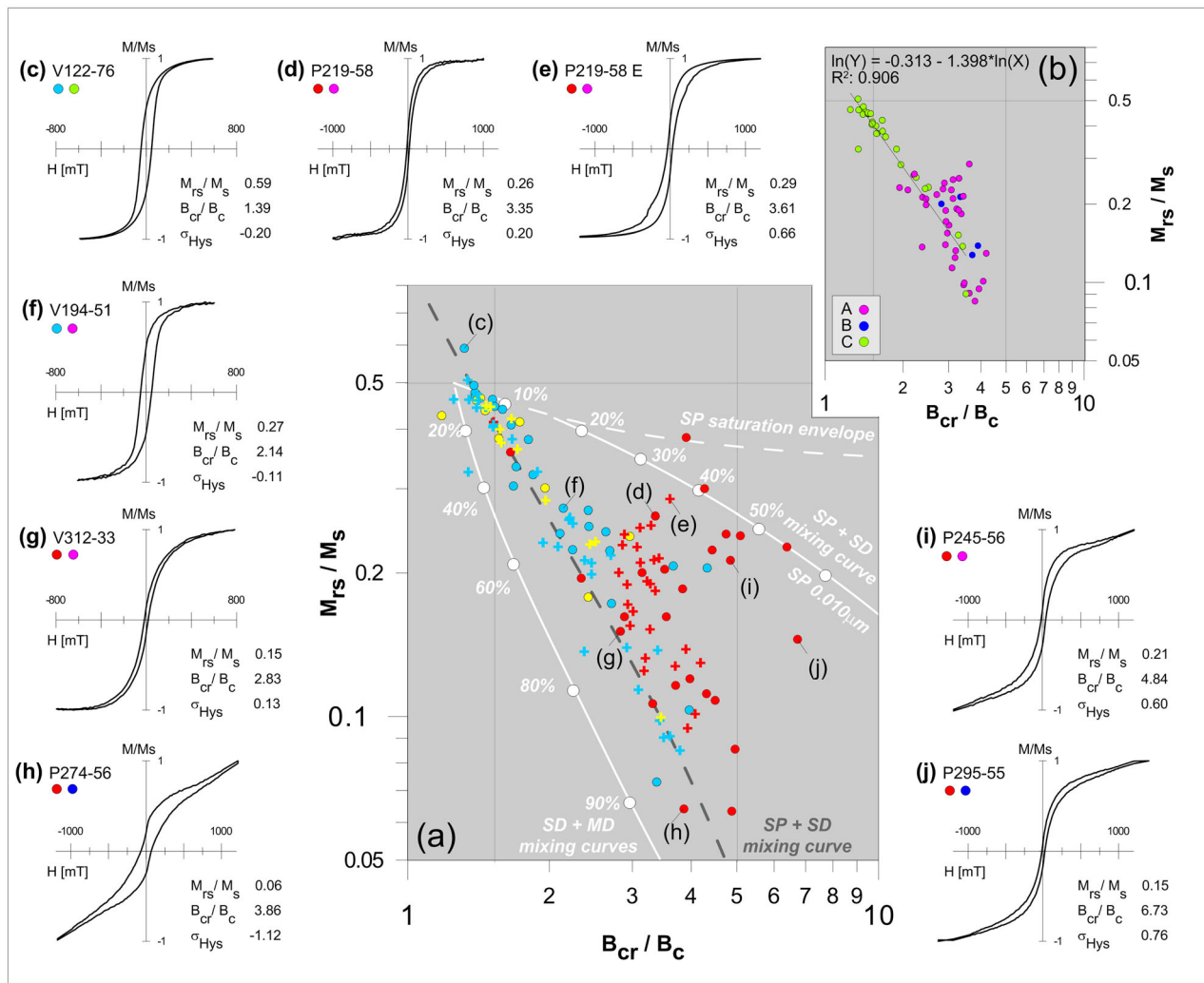


**Figure 8.** (a) Ratios of hysteresis parameters for bulk sample material (dots) and extracted material (crosses) of the Viernheim core and core P36 in Day plots (Day *et al.* 1977). Mixing lines for (titano)magnetite are drawn after Dunlop (2002a; white lines). Percentages indicate portions of SD particles. SD+SP trend line for binary mixing of greigite-bearing samples after Roberts *et al.* (2011; dark grey dashed line) is in good agreement with the samples from the Vfm and Lfm. Unit colour code follows that used in Fig. 1: green, Mfm; yellow, Lfm; blue, Vfm; red, IFm. (b) Day plot as in (a) showing only results from extracted materials, colour coded according to the different thermomagnetic groups. The trend line is calculated for C-type specimens of the Vfm and Lfm. (c–j) Exemplary hysteresis loops after paramagnetic correction. Filled circles below the label are related to the colour codes used in (a) and (b). All loops except (e) reflect bulk sample materials.

#### 4.4 Magnetic hysteresis

The representation of hysteresis parameters using Day plots (Day *et al.* 1977) are widely used for estimation of the mean domain state of magnetic mineral assemblages. Differences between the binary mixing curves of (titano)magnetites (Dunlop 2002a,b) and of greigite-bearing samples (Roberts *et al.* 2011) demonstrate the dependency of the magnetization and coercivity ratios on the composition of the sample material. Heslop & Roberts (2012) implemented a ternary mixing model with three end-members, demonstrating the difficulty of interpreting mixed mineralogy only on the basis of Day plots. Nevertheless, some clear trends can be recognized in the Day plots representing the results from 130 samples of magnetically extracted minerals and bulk sediment from the Viernheim and P36 cores (Fig. 8). The samples from the Heidelberg core were excluded from this analysis because they display excessive scattering.

The shapes of the hysteresis loops can be divided into three categories:

(1) Those compatible with a single magnetic mineral (e.g. magnetite) with domain states varying from a single-domain (SD) end-member (e.g. Fig. 8c) to a multi-domain (MD) end-member (e.g. Fig. 8g). These loops are characterized by hysteresis parameters that form a linear trend on the Day plots. This trend is located slightly above the SD-MD mixing curve predicted for magnetite by Dunlop (2002a; Fig. 8a).

(2) Due to the presence of high-coercive minerals, some loops are not saturated even in maximum fields of up to 1.8 T (e.g. Figs 8h and i). The slope increase in fields higher than 1 T is attributable to a spin-flop transition that occurs in antiferromagnetic minerals such as goethite and fine-grained haematite (Rochette *et al.* 2005). The hysteresis parameters of strongly unsaturated loops are meaningless, yielding Day plot parameters that depart significantly from

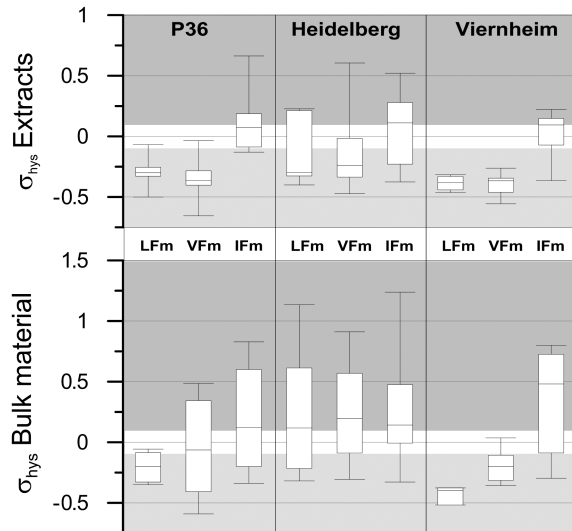


**Figure 9.** Variations in the  $\sigma_{\text{hys}}$  for cores and lithological units characterizing the shape of magnetic hysteresis loops. The widely scattered results of the Heidelberg core samples do not follow the trend shown by the other two cores. Note the different vertical axes for data from bulk material (lower part) and extracted material (upper part).

the general trend of most samples. For instance, the loop in Fig. 8(i) points to a 50:50 SP-SD mixture that is not supported by the frequency dependence of magnetic susceptibility.

(3) Finally, a third category of loops saturates in fields of  $\sim 1$  T but is characterized by a so-called wasp-waisted shape (Roberts *et al.* 1995; Tauxe *et al.* 1996), which is typical for binary mixtures of magnetic minerals with strongly contrasting coercivities (e.g. SD and MD or SD and SP) or a single phase affected by surface oxidation (Heisz & Hilscher 1987). Typical examples of such loops are shown in Figs 8(d) and (e). For the case of unsaturated loops, the hysteresis parameters of wasp-waisted loops tend to plot near the SD-SP mixing line of the Day plot, even though the corresponding samples do not contain significant amounts of SP materials, as indicated by the low frequency dependence of susceptibility discussed in Section 4.3.

The shapes of hysteresis loops are generally described by the parameter (Fabian 2003)

$$\sigma_{\text{hys}} = \ln \left( \frac{E_{\text{hys}}}{4M_S B_c} \right), \quad (2)$$

where  $E_{\text{hys}}$  is the area enclosed by the hysteresis branches,  $M_S$  is the saturation magnetization, and  $B_c$  is the coercivity.  $\sigma_{\text{hys}}$  quantifies the shapes of hysteresis loops by comparing  $E_{\text{hys}}$  with the area enclosed by an ideal rectangular loop with the same values of  $M_S$  and  $B_c$ . Wasp-waisted loops are characterized by  $\sigma_{\text{hys}} > 0$  and potbellied loops are characterized by  $\sigma_{\text{hys}} < 0$ .

All of the samples that plot near the SD-SP mixing line of the Day plot (Fig. 8a) are characterized by large values of  $\sigma_{\text{hys}}$  and are thus wasp-waisted. In particular, the IFm formation contains extreme examples (Figs 8i and j). Because strongly magnetic minerals, such as (titano)magnetite and greigite, are preferentially extracted, the disappearance of wasp-waisted signatures in magnetic extracts, as seen in the Day plot (Fig. 8b) and the  $\sigma_{\text{hys}}$  values (Fig. 9), implies the presence of high-coercive minerals with weak spontaneous magnetization (haematite, goethite). The IFm samples, in particular, are characterized by large amounts (by mass) of antiferromagnetic minerals. However, in a few cases, magnetic extraction does not lead

to a distinct decrease in  $\sigma_{\text{hys}}$  (e.g. Figs 8d and e). This observation can be explained by the intergrowth of low- and high-coercive phases, which are not separable by the extraction procedure. In contrast, samples from the VFm and the LFm show symmetrical to potbellied shapes (Fig. 9). Slightly constricted hysteresis loops occur only within the A-type bulk samples but not in the corresponding extracts, and thus probably also occur due to the presence of antiferromagnetic minerals.

The extracts from the VFm and the LFm define a mixing trend ( $R^2 = 0.906$ ), with the SD end-member being characterized by  $M_{\text{rs}}/M_s = 0.73$  at  $B_{\text{cr}}/B_c = 1$  (Fig. 8b). This trend is similar to that of greigite with  $M_{\text{rs}}/M_s = 0.81$  at  $B_{\text{cr}}/B_c = 1$  as the SD-end-member (Roberts *et al.* 2011). The properties of this end-member point to SD particles that are dominated by cubic anisotropy and have coercivity values compatible with those of greigite. Greigite is therefore the dominant ferrimagnetic component in samples from the VFm and the LFm; admixtures of other mineral phases probably generate the characteristic mixing trend seen in the Day plots (Figs 8a and b).

#### 4.5 FORCs

FORC diagrams (Pike *et al.* 1999; Roberts *et al.* 2000) provide additional details about the magnetization processes responsible for the hysteresis properties discussed in Section 4.4. Our measurements reveal a complex mixture of magnetic minerals with different domain states that correspond to the three types of thermomagnetic curves (A, B and C) discussed in Section 4.2. FORC diagrams of type-C samples are characterized by roughly elliptical FORC contours that define a broad peak centred at  $H_c = 50$ –60 mT and  $H_b = -5$  mT. This signature is indicative of greigite particles with relatively strong magnetostatic interactions that are produced by the typical growth habit of this mineral, which occurs in close-packed clusters (Roberts 1995, 2011).

The SD nature of this FORC signature is also confirmed by negative contributions in the lower-left corner of the diagrams (Figs 10d, f and i), which are partially truncated in some figures (Figs 10e and h). All greigite-dominated FORC diagrams also display variable contributions from a so-called central ridge, which is particularly evident in Fig. 10(b). This feature is a horizontal, sharp ridge extending along  $H_b = 0$  and is a characteristic signature of non-interacting SD particles (Newell 2005) that are commonly associated with magnetofossils in various types of marine and freshwater sediments (Egli *et al.* 2010; Ludwig *et al.* 2013; Heslop *et al.* 2014; Roberts *et al.* 2014). Central ridges do not necessarily originate from magnetofossils; a chemical origin is also possible. Differentiation of biological particles from authigenically precipitated minerals may be possible through analysis of the coercivity distribution associated with the central ridge. This requires isolating the central ridge from the remaining continuous contributions of the FORC diagram using the numerical methods implemented in VARIFORC (Egli *et al.* 2010; Ludwig *et al.* 2013). Although most of the diagrams have been obtained by averaging up to nine individual sets of measurements, the residual measurement noise is still too large to support such calculations, except for sample UN080-22, where the central ridge contributes  $\sim 2\%$  of the total remanent magnetization (Figs 10b and c). This central ridge contains two peaks at  $H_c = 10$ –20 mT and  $H_c = 70$  mT, respectively, of which the latter is compatible with the coercivity component 'BH' that is attributed to magnetofossils (Egli 2004a). The low-coercivity peak, on the other hand, is compatible with the expected coercivity distribution of isolated, nearly equidimensional SD magnetite particles (Maher 1988; Egli 2004c)

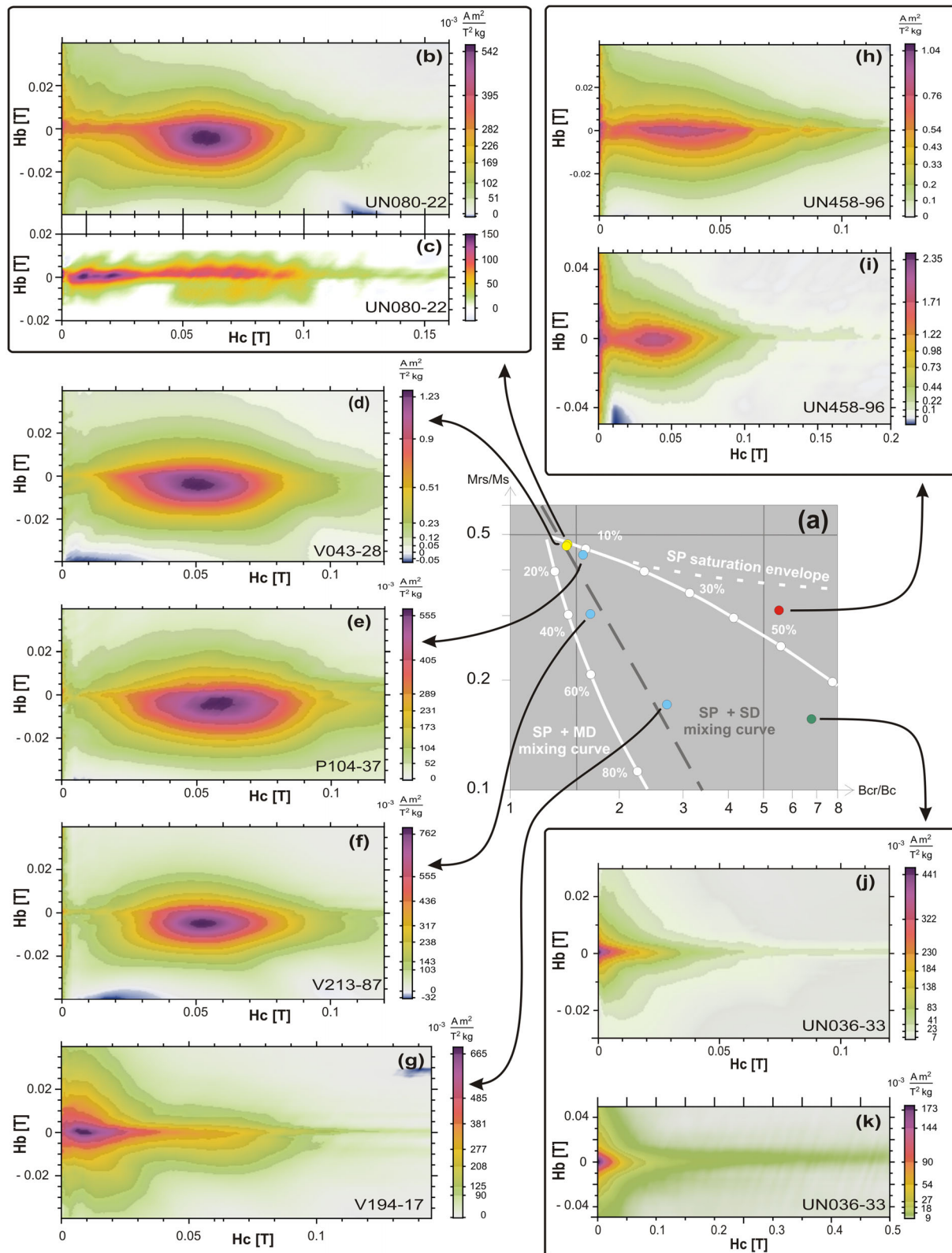


**Figure 10.** (a) Ratios of hysteresis parameters in the Day plot (Day *et al.* 1977). Mixing lines for magnetite (white) and greigite (grey) are drawn after Dunlop (2002a) and Roberts *et al.* (2011), respectively. Unit colour code follows that used in Fig. 1: green, MFm; yellow, LFm; blue, VFm; red, IFm. (b,d-k) FORC diagrams calculated with VARIFORC (Egli 2013) for data from multiple runs of each sample. (c) Extracted central ridge of sample UN080-22, which is shown in panel (b). (b-f) FORC diagrams for samples affiliated with thermomagnetic group C. Panel (g) shows an exceptional case; see the text for discussion. (h-k) FORC diagrams for samples affiliated with thermomagnetic group A. Panels (h) and (i), as well as (j) and (k), each shows measurements of the same sample. (h) and (j) are measured with the standard saturation field of 300 mT, whereas saturation fields of 800 and 1030 mT were applied for (i) and (k), respectively. Settings used to obtain the FORC measurements are listed in Table 1.

Caution should be applied in the interpretation of this central ridge, given its low magnetization ( $\sim 2\%$  of the bulk  $M_{rs}$ ) in comparison to that of magnetofossil-bearing sediments ( $>50\%$  of  $M_{rs}$ ; e.g. Kind *et al.* 2011; Heslop *et al.* 2013; Reinholdsson *et al.* 2013). In fact, the entire central ridge could be part of the greigite signature.

This hypothesis is supported by the fact that weak central ridges are clearly present in all greigite-bearing samples examined in this study and are also visible in high-quality FORC diagrams presented by other studies (e.g. Rowan & Roberts 2006).

FORC diagrams of C-type samples are further characterized by high-coercivity phases, which, along with results from thermomagnetic measurements, can be interpreted as originating from SD pyrrhotite particles (Wehland *et al.* 2005). Interestingly, the only greigite-bearing sample showing the additional low-coercivity FORC signatures that are usually associated with pseudo-single-domain (PSD) and MD magnetite particles is also sample UN080-22. We tentatively explain this fact by assuming that primary magnetite remainders are present to a greater extent than in the other samples. The magnetization of large magnetic minerals, which are highly diluted in the matrix of natural sample material, may be too small in relation to the main carriers to be depicted with the applied scale settings. Thus, the absence of PSD and MD signatures, for example in sample P104-37 (Figs 3b and 10e), is not necessarily inconsistent with the detection of large iron oxide grains by SEM/EDX. It should be borne in mind that those grains were preferentially extracted and identified with electron microscopy.

FORC diagrams of thermomagnetic type-A samples V194-17, UN458-96 and UN036-33 (Figs 10g–k) bear the typical signature of PSD magnetite, which consists of contour lines with increasing vertical spread at the zero-coercivity limit (e.g. Roberts *et al.* 2000; Muxworthy & Dunlop 2002). This is especially clear in the case of UN036-33, where the only additional FORC signature is that of a high-coercivity central ridge that will be discussed later. Surprisingly, other A-type samples seem to contain variable amounts of greigite, as in sample V213-87 (Fig. 10f).

In general, the presence of greigite in A-type samples gives an important clue to the highly variable resistance of this mineral to oxidation during the extraction procedure. Some FORC diagrams, such as V194-17 (Fig. 10j) and UN458-96 (Fig. 10h), clearly result from the superposition of two phases with PSD and greigite-like end-member properties.

Finally, the last FORC signature identifiable in our samples is a high-coercivity central ridge (Figs 10i and j). This ridge extends well beyond the coercivity range of magnetite and greigite, and appears to be associated with extremely hard SD particles, as shown in high-resolution FORC measurements to  $H_c = 0.5$  T (Fig. 10k).

The high-coercivity central ridge is attributable to SD haematite and/or goethite particles with switching fields that are significantly lowered by thermal activation. The origin of these particles is not known. Geological observations clearly suggest different haematite sources, for example, denudation of Triassic red beds in sample UN036-33 and authigenic growth in UN458-96 (Ellwanger *et al.* 2008).

#### 4.6 Coercivity analysis

Coercivity analyses unravel the full complexity of the investigated sediment by identification of 30 components, of which as many as five occur simultaneously (Table 3). The components are attributable to the presence of different minerals discussed below, and can be grouped into six strongly overlapping coercivity ranges (Table 3 / Fig. 11) The association of individual coercivity

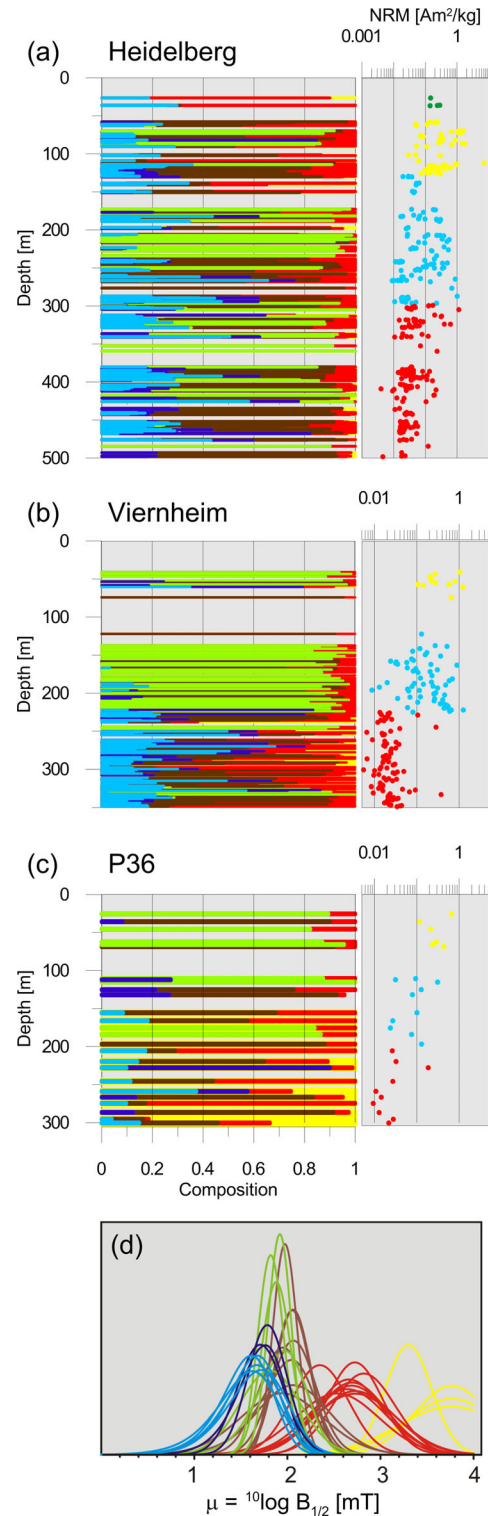


**Figure 11.** (a–c) Composition (left) and NRM values (right) of individual samples from the cores. Compositions are indicated by colour-coded bars that show the relative portions of the respective magnetic mineralogy. Azure blue: magnetites and chromite; navy blue: magnetites and sulphides; green: sulphides; brown: sulphides and haemo-ilmenites; red: haematite; yellow: goethite. For details, see text. Unit colour code of NRM values follows that used in Fig. 1: green, MFm; yellow, LFm; blue, VFm; red, IFm. (d) Components used for modelling of the natural sample materials.

**Table 3.** Components determined using coercive analysis in the Mag-Mix software package (Egli 2003, 2004a), arranged in clusters.

Component	no	$\mu$	$B_{1/2}$ (mT)	$\sigma$	$s$	$P$
RC01-1	53	1.933	85.70	0.291	0.66	2.00
RC01-2	53	1.914	81.98	0.127	1.00	2.00
RC01-3	52	2.643	439.89	0.418	1.00	2.00
RC02-1	37	2.662	459.71	0.364	1.00	2.00
RC02-2	37	2.051	112.50	0.190	0.96	2.00
RC02-3	36	1.707	50.94	0.296	0.60	2.10
RC03-1	45	1.813	65.02	0.326	1.00	2.00
RC03-2	45	1.880	75.93	0.159	1.00	2.00
RC03-3	38	2.534	342.37	0.447	1.00	2.00
RC04-1	44	2.819	659.72	0.338	0.95	2.00
RC04-2	44	1.974	94.18	0.130	1.00	2.00
RC04-3	44	1.984	96.43	0.338	0.59	2.00
RC05-1	74	1.709	51.23	0.249	1.00	2.00
RC05-2	74	1.942	87.41	0.441	1.00	1.94
RC05-3	72	3.300	1995.26	0.250	0.95	2.00
RC05-4	71	2.724	529.71	0.297	0.95	2.00
RC06-1	23	1.563	36.54	0.373	0.62	2.00
RC06-2	26	1.950	89.18	0.256	0.95	2.00
RC06-3	26	2.694	494.41	0.380	0.95	2.00
RC07-1	19	2.687	486.49	0.397	0.95	2.00
RC07-2	19	2.064	115.98	0.240	1.00	2.00
RC07-3	19	1.561	36.40	0.316	0.62	2.00
RC08-1	59	2.062	115.33	0.189	1.00	2.00
RC08-2	64	1.624	42.08	0.316	0.62	2.00
RC08-3	64	2.726	532.48	0.450	0.95	2.00
RC08-4	9	3.763	5793.75	0.398	0.95	2.00
RC09-1	108	1.624	42.08	0.339	0.65	2.00
RC09-2	112	2.062	115.33	0.394	1.00	2.00
RC09-3	27	1.820	66.11	0.138	0.95	2.00
RC09-4	57	3.763	5793.75	0.490	0.95	2.00
RC09-5	111	2.726	532.48	0.431	0.95	2.00
RC10-1	30	3.763	5793.75	0.569	0.95	2.00
RC10-2	32	1.670	46.76	0.358	0.65	2.00
RC10-3	32	1.785	60.94	0.211	1.00	2.00
RC10-4	33	2.349	223.38	0.306	1.00	2.00

Note: Number of occurrences (no) and parameters ( $\sigma$ ,  $\mu$ ,  $s$ ,  $p$ ).

distributions with certain mineral components is only possible with additional mineralogical information, such as thermomagnetic behaviour (groups A, B and C), EDX analysis, and FORC measurements.

All coercivity components with median fields  $B_{1/2} < 47$  mT ( $\mu = 1.670$ , shown in light blue in Fig. 11) are left-skewed distributions with  $\sigma$ -values in the range of 0.316–0.373. Several studies (e.g. Kruiver *et al.* 2001; Hüsing *et al.* 2009; Dennie *et al.* 2012; Just *et al.* 2012) interpreted these components as related to (impure) detrital magnetites with a wide range of grain sizes and oxidation states. Furthermore, maghemite, ferrochromite and, relatively low-coercive minerals from the haematite-ilmenite series may be involved (Kumar & Bhalla 1984; Robertson & France 1994; Grygar *et al.* 2003; Egli 2004a; Schnabl *et al.* 2010; Brownlee *et al.* 2011). The contribution of these components to the SIRM reaches 74%, making them the dominant remanence carrier. As seen from the weak NRM of most samples, the concentration is low, especially in the Viernheim and P36 cores, where these minerals mainly occur in the IFm. The coercivity spectra of these magnetite-like minerals overlap in the coercivity range between  $B_{1/2}$  51 mT and 61 mT

**Table 4.** Components arranged in order of ascending  $\mu$  values, neglecting variances in  $\sigma$ .

$B_{1/2}$ [mT]	$\mu$		no
36.40	1.561		19
36.54	1.563		23
42.08	1.624		172
46.76	1.670		32
50.94	1.707		36
51.23	1.709		74
60.94	1.785		32
65.02	1.813		45
66.11	1.820		27
75.93	1.880		45
81.89	1.914		53
85.70	1.933		53
87.41	1.942		74
89.18	1.950		26
94.18	1.974		44
96.43	1.984		44
112.50	2.051		37
115.33	2.062		171
115.98	2.064		19
223.38	2.349		33
342.37	2.534		38
439.89	2.643		52
459.71	2.662		37
486.49	2.687		19
494.41	2.694		26
529.71	2.724		71
532.48	2.726		175
659.72	2.819		44
1995.26	3.300		72
5793.75	3.763		96

Number of occurrences (no). Colour code as in Fig. 11: Azure blue: magnetites and chromite; navy blue: magnetites and sulphides; green: sulphides; brown: sulphides and haemo-ilmenites; red: haematite; yellow: goethite.

( $\mu = 1.707$ – $1.785$ , shown in dark blue in Fig. 11) with those of sulphides (discussed below); thus, the peaks cannot be attributed to one of these mineral groups with certainty.

A major group of components is characterized by  $B_{1/2}$ -values ranging from 65 to 86 mT ( $\mu = 1.813$ – $1.933$ , green in Fig. 11). Frequently, two of these components can be identified within the same sample (clusters RC1 and RC3 in Tables 3 and 4). These pairs consist of one component with small  $\sigma$  (not exceeding 0.16) and one with larger  $\sigma$  (between 0.29 and 0.33) and carry on average ~90% of the bulk SIRM; the associated samples show the largest NRM values of all of the sections. Furthermore, all of the samples with strong contributions from these components are characterized by type-C thermomagnetic curves, which, as seen in Sections 4.4 and 4.5, are typical of iron sulphides. Similar combinations of coercivity components are interpreted as representing the co-occurrence of greigite magnetofossils and authigenic greigite (Vasiliev *et al.* 2008; Hüsing *et al.* 2009). The results of this study can appropriately be compared to those of Vasiliev *et al.* (2008); the contribution to  $M_{rs}$  of the component with small and large  $\sigma$  is 31%–48% and ~50%, respectively (median values). In addition, the FORC diagram of sample UN080-22 closely resembles the one shown in Vasiliev

*et al.* (2008). However, there are reasons not to attribute the narrow coercivity peak to greigite magnetofossils here. Contrary to Vasiliev *et al.* (2008), high resolution FORCs were applied and revealed that the central ridge contribution of UN080-22 does not exceed 2% of  $M_{rs}$ . In addition, UN080-22 is composed of a higher coercive pair of components (cluster RC04) that fall within the subsequent range with  $B_{1/2} = 87$  mT to 116 mT ( $\mu = 1.942\text{--}2.064$ , brown in Fig. 11). The properties of the components in this range vary strongly in every respect and are probably also related to oxides and sulphides.

Taken as a whole, the interpretation of the components in the  $B_{1/2}$  range between 51 and 116 mT leaves many open questions. The components with larger  $\sigma$ -values probably include unquantifiable proportions of harder magnetites (Kruiver & Passier 2001; Liu *et al.* 2007), pyrrhotite (Clark 1984) and minerals from the ilmenite-haematite series (McEnroe *et al.* 2002; Brownlee *et al.* 2011). It should be borne in mind that previous sections have shown that these minerals co-occur with greigite. The unusually narrow coercivity distributions and relatively high coercivities of some components point towards SD magnetic particles with very uniform properties; possible candidates are magnetofossils (e.g. component BH in Egli 2004a), both magnetite (elongated) and greigite, or quasi-ordered structures such as framboidal greigite aggregates (Rowan & Roberts 2006), whose intrinsic FORC signature appears to be similar to that of UN080-22. None of these interpretations appears to fit all of the observed magnetic properties with our current knowledge; magnetofossils lack an appropriately large central ridge signature in FORC diagrams, and greigite magnetosomes are characterized by  $B_{1/2} = 20\text{--}35$  mT (Winklhofer *et al.* 2014). The coercivity argument holds also for authigenic greigite; the larger cubic magnetocrystalline anisotropy ( $17\text{--}26$  kJ m<sup>-3</sup>, compared to magnetite's  $2.8$  kJ m<sup>-3</sup> (Winklhofer *et al.* 2014) yields coercivities in the order of  $40\text{--}50$  mT. However, cation impurities in natural greigite, as well as unrecognized pyrrhotite lamellae, could increase the coercivity to the observed values (Winklhofer *et al.* 2014). The pyrrhotite lamellae hypothesis is supported by the presence of a positive internal bias field, which produces a downward shift of the central FORC maximum of greigite-bearing samples (Fig. 10). A magnetostatic origin of such a positive field appears unlikely, since it requires a type of loose, chain-like arrangement of SD particles that could only originate from magnetosome chains. However, magnetofossil-bearing sediments are never characterized by measurable internal bias fields (Egli *et al.* 2010; Ludwig *et al.* 2013). In conclusion, the most likely origin of the narrow coercivity components with  $B_{1/2} = 60\text{--}100$  mT is related to authigenic greigite with various degrees of cation substitution and/or pyrrhotite lamellae.

The remaining groups of coercivity components are characterized by  $B_{1/2}$  values ranging from  $\sim 220$  to  $\sim 530$  mT (shown in red in Fig. 11d) and  $B_{1/2} > 659$  mT (shown in yellow in Fig. 11d), respectively. Because of their large coercivity, these components are generally not saturated, contributing significant uncertainty to the corresponding parameters. We expect minerals from the solid solution series from ilmenite to haematite to be associated with the components in the lower part of this coercivity range. For comparison, haematite coercivity distributions peak between 350 and 1000 mT as a function of grain size, stress, and chemical variations (Robertson & France 1994; Kruiver & Passier 2001; Kletetschka & Wasilewski 2002; Liu *et al.* 2011; Dennie *et al.* 2012). Haematite can thus explain the intermediate components of this group. Finally, ultrahigh coercivity components are associated with goethite (France & Oldfield 2000). If components from this group are dominant, the NRM is generally low.

The overall distribution patterns of the components confirm that the succession reflected by the Heidelberg core had a different genesis than those of the other two cores. Whereas the Viernheim and P36 cores are characterized by the almost mutually exclusive occurrence of either greigite or a mixture of low-coercivity magnetite and high-coercivity phases, all of the coercivity components occur in various proportions over almost the entire Heidelberg succession. This can be explained by its proximity to the graben shoulders and the influence of the Neckar River. A continuous delivery of red bed sediments from the hinterland into the Heidelberg area was provided by the Neckar and other streams. In addition, the interaction of continuous and strong subsidence and a steady water supply likely led to a situation in which reducing conditions prevailed and sulphides survived.

## 5 DISCUSSION

### 5.1 Magnetic mineralogy and environmental implications

Rock magnetic investigations reveal the presence of complex mixtures of iron oxides and sulphides, which point towards a complex formation history of the Heidelberg Basin sequences.

The mineralogical composition, as well as the distribution pattern of the mottled colour variations in the Pliocene-age IFm, point to alternation of oxidizing and reducing conditions during deposition and early diagenesis (Bown & Kraus 1987; Kraus 1999, 2002). The sediments were mainly delivered from the graben shoulders and were thus primarily composed of a high proportion of stable minerals (Hagedorn & Boenigk 2008). Upon deposition, the sediments underwent reducing diagenesis, followed by an oxidizing phase that was probably caused by repeated lowering of the groundwater table during seasonal or supra-seasonal (sub-orbital to orbital) climatic cycles. Largely humid climates gave rise to prevalent reducing conditions in which pyrite and greigite formed. Finally, the occurrence of haematite pseudo-morphs after pyrite and the slightly pitted surfaces of haematite suggest an alternating sequence of oxidizing and reducing conditions, during which Cr-spinels (Cr-magnetites) and ilmenites became concentrated due to their resistance to dissolution and replacement (Milliken & Mack 1990; Hounslow 1996; Maher & Hallam 2005). The present appearance of the sediments exhibits pervasive oxidation of discrete horizons, as reflected by the dominance of haematite and goethite and by the occurrence of pedogenic pisolites. The haematite likely developed in arid conditions by the transformation of reactive iron into magnetite, maghemite and finally into haematite and from the oxidation of detrital precursors, respectively (e.g. Stacey & Banerjee 1974; Turner 1980; de Boer & Dekkers 1996; Dunlop & Özdemir 1997). Generally, the dissolution and/or conversion of detrital magnetic minerals become apparent by their only occasional appearance in SEM/EDX analyses and relatively low susceptibility (Fig. 7) and NRM values (Fig. 11). The magnetite-like signal observed in the thermomagnetic measurements and coercivity analyses is thus related to ferrimagnetic inclusions, which probably carry an appreciable part of the total magnetization.

The greigite and pyrite in the IFm sediments of the Viernheim and P36 drill cores were probably destroyed during oxidizing events. The frequently observed viscous magnetizations (Scheidt *et al.* 2015) may arise from such oxidation processes (Rowan & Roberts 2006). If any, greigite seems to remain only in trace amounts. Since no sulphides were found in the SEM/EDX analyses, pyrite might have survived in the cores of oxidized grains, thus explaining the

thermomagnetic measurements of the IFm extracts. In contrast, pyrite and its precursor greigite are preserved to a far greater extent in the sediments of the Heidelberg core, which presumably endured less frequent oxidizing events. A substantial part of the differences between the rock magnetic parameters of the IFm in the Heidelberg core on the one hand and the Viernheim and P36 cores on the other hand are due to the presence or absence of greigite.

The Plio-Pleistocene-boundary is located in the uppermost part of the IFm (Scheidt *et al.* 2015) and coincides with a time interval characterized by major climate changes and that also featured an extension of the catchment of the Rhine River (Preusser 2008). Accordingly, the mineral composition of the sediments from the VFm and the LFm indicate a different evolution of these Pleistocene units. In contrast to the IFm, the occurrences of haematite in the Pleistocene strata are attributed to the input of detrital material from the Neckar and the graben shoulders. Signs of authigenic formation have not been found. The Heidelberg core is particularly heavily affected by these denudation products of the Triassic hinterland, which led to a Pleistocene mineral association with significant amounts of high-coercivity constituents.

In all of the cores, the abundance of greigite indicates continued saturation of the sediment column with water, leading to overall steady reducing conditions. However, the time of formation of this mineral and the mechanism of its preservation is complex and not easily determined. A comprehensive overview of the relevant processes and key factors is provided in the literature (e.g. Heywood *et al.* 1991; Hoffmann 1992; Fassbinder & Stanjek 1994; Roberts 1995; Wilkin & Barnes 1997; Chang *et al.* 2009; Roberts *et al.* 2011, 2015). For the purpose of this study, the following observations are important.

Although narrow coercivity distribution peaks are usually reported for magnetofossil components (Kruiver & Passier 2001; Egli 2004a,c), the bulk rock magnetic parameters (e.g.  $\chi$ ARM/IRM (Moskowitz *et al.* 1993), not shown) and the lack of pronounced central ridges in the FORC diagrams are compatible with the signature of authigenic greigite. We postulate a detrital origin for most of the pyrrhotite in the Heidelberg Basin, since an authigenic origin implies unusually high pH values (> 11) and elevated temperatures (~180 °C; Garrels & Christ 1965). Outcrops of suitable igneous and metamorphic source rocks are located in the nearby Odenwald (Ramdohr 1975). Transportation from the distal Alps also appears to have been possible, if the pyrrhotite were enclosed in minerals or mineral aggregates. Finally, minor amounts of authigenic pyrrhotite might occur as intergrowths with greigite, explaining the downward shift of the central maximum of the FORC diagrams of greigite-bearing samples.

The preservation of both sulphides points towards high accumulation rates, since detrital pyrrhotite is preserved from oxidation only if fast erosion is combined with rapid transportation and burial (e.g. Horng *et al.* 1998; Weaver *et al.* 2002; Horng & Roberts 2006; Hu *et al.* 2006; Roberts 2015). In the case of greigite, the availability of reactive iron, organic carbon, and reduced sulphur determines whether pyritization occurs, or whether the reaction ends with the precursor minerals. High accumulation rates and rapid burial limit the availability of the reactants, thus enabling the preservation of greigite (Berner 1970; Kao *et al.* 2004). In this respect, the identification of fragile magnetite remainders indicate that no shortage of iron occurred in those layers.

Furthermore, the presence of magnetic sulphide-free horizons with A-type thermomagnetic curves within sulphidic sections can also be explained by sudden depositional events that prevented pervasive reducing diagenesis.

The top layers may have been buried by sediment packages, restricting the availability of reactive sulphur and organic carbon. However, the existence of some of these A-type horizons caused by the oxidative loss of sulphide minerals, whether in situ or during storage after drilling, cannot be ruled out. Those processes are eventually associated with loss of susceptibility in the dark clayey layers, as described in Section 4.3. In contrast, the intact habitus of minerals in some of the sandy sections and the occurrence of magnetite placers suggest prevailing non-reducing conditions.

The general lack of superparamagnetic behaviour indicates an extensive loss of fine-grained ferrimagnetic minerals, sulphides as well as oxides, which probably occurred during reducing diagenesis. In addition, both, greigite and magnetite are prone to be transferred into goethite or other oxyhydroxides under oxidizing and humid conditions (e.g. Taylor *et al.* 2014).

Finally, the gravelly and coarse sandy sediments that are predominant within the MFm prevent meaningful interpretation of the magnetic mineralogy of this lithostratigraphic unit.

## 5.2 Reliability of palaeodirections carried by the detected minerals

The ability of magnetite-poor sediments to carry palaeomagnetic signals is still debated, especially with respect to the possibility that significant portions of the magnetic signal are carried by magnetic iron sulphides or haematite (e.g. Tauxe & Kent 1984; Rösler *et al.* 1997; Liu *et al.* 2003; Horng & Roberts 2006; Sagnotti *et al.* 2010; Nilsson *et al.* 2013). The possibility that these minerals formed long after deposition can greatly affect their magnetic recording reliability. Such problematic minerals are abundant in the sediments of the Heidelberg Basin.

The magnetic mineral assemblage of the IFm is mainly composed of Fe(-Ti) chromites, magnetite, (haemo)ilmenite, and high-coercive minerals, of which haematite makes up an important part of the majority of the samples (Tables 3 and 4).

The ability of (haemo)ilmenite and Fe(-Ti) chromites to retain stable detrital remanent magnetization (DRM) over geologically relevant times has been shown by several studies (e.g. Kumar & Bhalla 1984; Lawson & Nord 1984; Nord & Lawson 1989; Hounslow *et al.* 1995; Hounslow & Maher 1996; Maher & Hallam 2005).

Based on the suggested authigenic haematite formation pathway, the recorded palaeodirections are also considered to be reliable: the surface-bound transformation of minerals into haematite occurred on the steadily subsiding floodplains of the proto-Rhine. Even though the deposited sediments might have been eroded or reworked, the formation of haematite was stopped by burial; thus, the preserved signals represent palaeomagnetic directions of the respective top layers (pDRM).

Finally, magnetites carry a part of the remanence in certain layers of the IFm. If prolonged reducing diagenesis dissolved the SD and PSD grain size fraction completely, no synsedimentary palaeomagnetic signal can be preserved. If, however, minor dissolution features indicate insignificant chemical alteration, magnetites in certain grain sizes may retain a stable palaeodirection, even after partial oxidation (Karlin & Levi 1983; Ge *et al.* 2014). Magnetite and Ti-magnetite inclusions in ilmenite and other host minerals may also carry a reliable palaeomagnetic signal (Hounslow *et al.* 1995).

The palaeomagnetic reliability of iron sulphides is more difficult to assess. While some authors caution against the possibility of late greigite genesis (e.g. Florindo & Sagnotti 1995; Jiang *et al.* 2001;

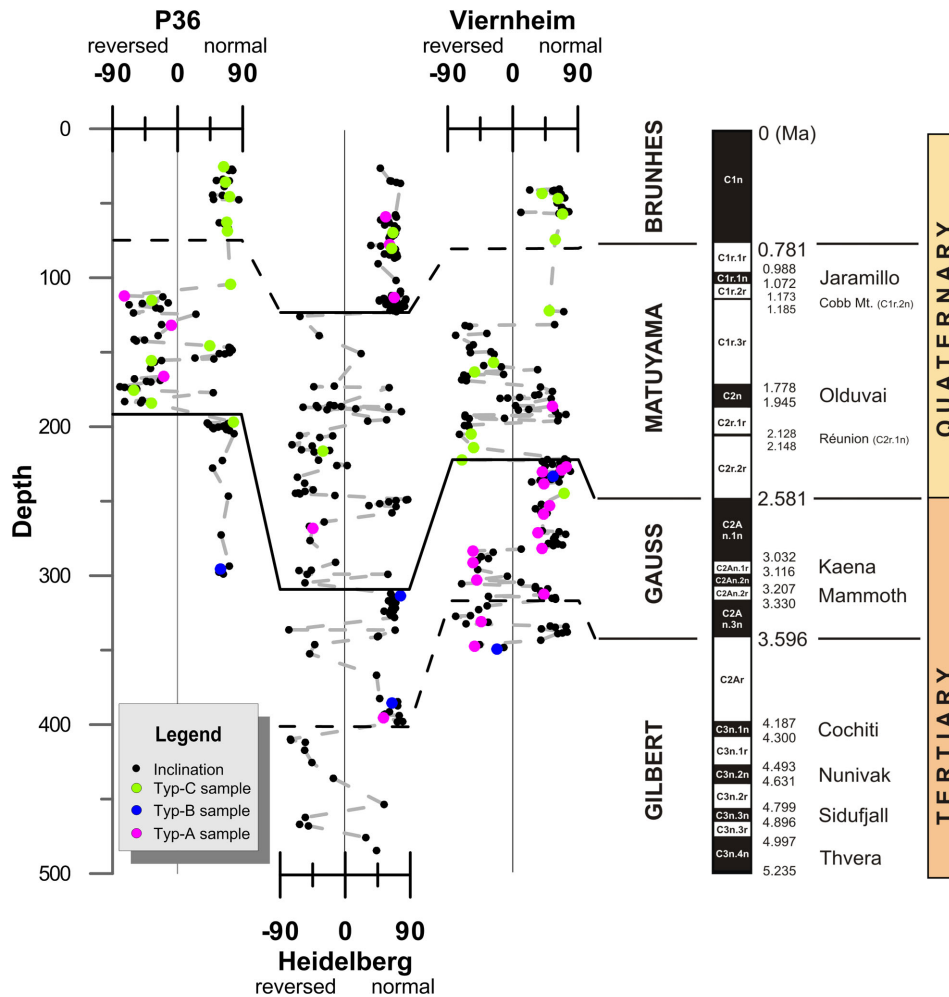


**Figure 12.** Inclination values and deduced correlations with the geomagnetic polarity time scale (GPTS), as shown in Scheidt *et al.* (2015). GPTS after Cande & Kent (1995), as shown in Ogg *et al.* (2016). Inclination values are indicated by thermomagnetic group affiliation, as in Fig. 8: pink, group A; blue, group B; green, group C; or by black filled dots if no thermomagnetic measurements were performed. Correlation lines are shown as solid lines and dashed lines for clear and inconclusive positions, respectively. The latter cases result from data gaps (for details, see Scheidt *et al.* 2015).

Weaver *et al.* 2002; Roberts & Weaver 2005; Sagnotti *et al.* 2005; Rowan *et al.* 2009), others report a stable pDRM that is related to an early diagenetic origin of this mineral (Canfield & Berner 1987; Reynolds *et al.* 1999; Babinszki *et al.* 2007; Frank *et al.* 2007; Vasiliev *et al.* 2007). In addition, the rate of in situ greigite nucleation and growth ranges from a few years to thousands of years (Pye 1981; Canfield & Berner 1987; Reynolds *et al.* 1999).

Palaeomagnetic information from the Heidelberg basin should be evaluated carefully, considering that the geological settings are characterized by episodic accumulation and erosion events. The magnetostratigraphy was obtained from samples selected after the application of stringent quality criteria that were created with the aim of isolating the characteristic remanent magnetization (for details see Scheidt *et al.* 2015). The resultant polarity stratigraphy does not show any correlation with the magnetic mineralogy, as indicated by the thermomagnetic group affiliations (Fig. 12). In particular, the coincidence of DRM-carrying samples (A-type thermomagnetic properties) and samples which contain authigenic minerals (B- and C-type thermomagnetic curves) indicates the formation of pDRM-carrying authigenic minerals shortly after deposition. The insignificant occurrence of some layers showing mixed (normal and reverse) polarity within the normal Olduvai and Jaramillo events,

as recorded in the Viernheim core and the Heidelberg core, respectively (Fig. 12; *cf.* Scheidt *et al.* 2015), likely results from late mineral formation but does not impair the overall good results.

## 6 CONCLUSIONS

The combined results of rock magnetic analyses and SEM/EDX observations demonstrate that meaningful results can be obtained from unconsolidated, fluvial dominated sedimentary successions from the Plio-Pleistocene of the URG. It has been shown that the interpretation of the magnetic mineralogy is very complex, due to the simultaneous occurrence of several magnetic components. In this study, the combination of EDX/SEM, thermomagnetic measurements, CLG curves and FORC diagrams enable the identification of up to five coexisting magnetic components. In contrast, bulk magnetic parameters were only able to depict general trends in terms of bulk coercivity, for example. The effects of magnetic grain size variations were superimposed by the stronger effects of the natural variances of the components; thus, these variations cannot be assessed.

The reconstructed magnetic mineralogy provides insights into the complex history of evolution of this basin, which can be

summarized as follows. The Tertiary-age IFm underwent recurrent reductive diagenesis and subsequent oxidation events. Accordingly, most of the magnetite grains dissolved or transformed into haematite and goethite. Greigite and pyrite survived only under the moist conditions and higher accumulation rates found in the centre of subsidence (Heidelberg) and have been almost entirely oxidized in other locations within the basin. The IFm retains a primary DRM that is carried by ferrian ilmenites, titanomagnetite, Cr-Fe spinels, and impure magnetites. The haematite holds a pDRM/CRM (chemical remanent magnetization) and imparts the distinctive colour to the sediments.

During the accumulation of the Pleistocene-age VFm and LFm, reducing conditions continued, and these conditions persisted during diagenesis. Thus, sulphides became the main remanent magnetization carriers. The magnetites were preserved mainly because of sudden sedimentation events that restricted the availability of sulphate or organic matter. An insufficient supply of these reactants must also have stopped the pyritization process, leading to the preservation of initially formed greigite and pyrrhotite over geological time. Magnetite and greigite magnetofossils are practically absent.

In summary, meaningful rock magnetic and palaeomagnetic results could be obtained, despite the heterogeneous and complex composition of the sediments and the enormous volume of the analysed sample set. These results enable us to disentangle the magnetic mineral compositions of fluvial dominated environments and to confirm the reliability of the magnetic polarity stratigraphy of the Heidelberg Basin (Scheidt *et al.* 2015). The combination of techniques used in this study may provide a template for future fluvial basin analyses.

## ACKNOWLEDGEMENTS

This study was funded by the German Research Foundation DFG (RO2170/8-1, RO2170/8-2, HA2193/10-1 and HA2193/10-2). We are grateful to Lena Wallbrecht, Kathrin Worm and Sabine Stäger for technical assistance in the labs of Grubenhagen and Hannover, respectively. Dr. Eduard Petrovsky enabled us to continue work in the rock magnetic laboratory of the Institute of Geophysics, Academy of Sciences (Czech Republic, Prague) during times of equipment failure. Dr. Stefan Kaufhold gave helpful advice in questions of mineral identification. We also wish to thank the anonymous reviewers who have helped to improve the manuscript.

## REFERENCES

- Ahmed, S.S., Miah, M.Y., Qumruzzaman, C., Zaman, M.N., Alam, A.B. & Biswas, P.K., 2010. Alteration and exsolution characteristics of ilmenites of Mohekhali Island, Chittagong, Bangladesh, *Bangladesh J. Sci. Ind. Res.*, **45**, 17–26.
- Babinski, E., Márton, E., Márton, P. & Kiss, L.F., 2007. Widespread occurrence of greigite in the sediments of Lake Pannon: Implications for environment and magnetostratigraphy, *Palaeogeogr. Palaeoclimatol. Palaeoecol.*, **252**, 626–636.
- Bartz, J., 1959. Gliederung des Pleistozäns im Oberrheingebiet, *Z. Dtsch. Geol. Ges.*, **111**, 739–781.
- Bartz, J., 1974. Die Mächtigkeit des Quartärs im Oberrheingraben, *Approaches to Taphrogenesis*, **8**, 78–87.
- Bartz, J., 1976. Quartär und jungtertiär im raum rastatt, *Jh geol Landesamt Baden-Württemberg*, **18**, 121–178.
- Bartz, J., Von, M.B., Breilie, G. & Maus, H., 1982. Quartär und Jungtertiär II im Oberrheingraben im Großraum Karlsruhe, *Geol. Jb. A, Bd.*, **A63**, 3–237.
- Bernal, J., Dasgupta, D. & Mackay, A., 1957. Oriented transformations in iron oxides and hydroxides, *Nature*, **180**, 645–647.
- Berner, R.A., 1970. Sedimentary pyrite formation, *Am. J. Sci.*, **268**, 1–23.
- Biswas, D.K., Hyodo, M., Taniguchi, Y., Kaneko, M., Katoh, S., Sato, H., Kinugasa, Y. & Mizuno, K., 1999. Magnetostratigraphy of Plio-Pleistocene sediments in a 1700-m core from Osaka Bay, southwestern Japan and short geomagnetic events in the middle Matuyama and early Brunhes chrons, *Palaeogeogr. Palaeoclimatol. Palaeoecol.*, **148**, 233–248.
- Bloemendal, J., King, J., Hall, F. & Doh, S.J., 1992. Rock magnetism of Late Neogene and Pleistocene deep-sea sediments: relationship to sediment source, diagenetic processes, and sediment lithology, *J. geophys. Res.*, **97**, 4361–4375.
- Bown, T.M. & Kraus, M.J., 1987. Integration of channel and floodplain suites. I. Developmental sequence and lateral relations of alluvial paleosols, *J. Sediment. Res.*, **57**, 587–601.
- Brownlee, S.J., Feinberg, J.M., Kasama, T., Harrison, R.J., Scott, G.R. & Renne, P.R., 2011. Magnetic properties of ilmenite-hematite single crystals from the Ecstall pluton near Prince Rupert, British Columbia, *Geochem. Geophys. Geosyst.*, **12**, Q07Z29, doi:10.1029/2011GC003622.
- Buness, H., Gabriel, G. & Ellwanger, D., 2008. The Heidelberg Basin drilling project: Geophysical pre-site surveys, *E & G (Quat. Sci. J.)*, **57**, 338–366.
- Cande, S.C. & Kent, D.V., 1995. Revised calibration of the geomagnetic polarity timescale for the Late Cretaceous and Cenozoic, *J. geophys. Res.*, **100**(B4), 6093–6095.
- Canfield, D.E. & Berner, R.A., 1987. Dissolution and pyritization of magnetite in anoxic marine sediments, *Geochim. Cosmochim. Acta*, **51**, 645–659.
- Chang, L., Roberts, A.P., Rowan, C.J., Tang, Y., Pruner, P., Chen, Q. & Horng, C.S., 2009. Low-temperature magnetic properties of greigite (Fe<sub>3</sub>S<sub>4</sub>), *Geochem. Geophys. Geosyst.*, **10**, Q01Y04, doi:10.1029/2008GC002276.
- Clark, D., 1984. Hysteresis properties of sized dispersed monoclinic pyrrhotite grains, *Geophys. Res. Lett.*, **11**, 173–176.
- Da Costa, G., De Grave, E., Bowen, L., De Bakker, P. & Vandenberghe, R., 1995. Temperature dependence of the hyperfine parameters of maghemite and Al-substituted maghemites, *Phys. Chem. Miner.*, **22**, 178–185.
- Day, R., Fuller, M. & Schmidt, V.A., 1977. Hysteresis properties of titanomagnetites; grain-size and compositional dependence, *Phys. Earth planet. Inter.*, **13**, 260–267.
- Dearing, J., 1999. Holocene environmental change from magnetic proxies in lake sediments, in *Quaternary Climates, Environments and Magnetism*, pp. 231–278, eds Maher, B.A. & Thompson, R., Cambridge Univ. Press.
- De Boer, C.B. & Dekkers, M.J., 1996. Grain-size dependence of the rock magnetic properties for a natural maghemite, *Geophys. Res. Lett.*, **23**, 2815–2818.
- De Boer, C.B., Dekkers, M.J. & Van Hoof, T.A.M., 2001. Rock-magnetic properties of TRM carrying baked and molten rocks straddling burnt coal seams, *Phys. Earth planet. Inter.*, **126**, 93–108.
- Dekkers, M., 1989. Magnetic properties of natural pyrrhotite. II. High- and low-temperature behaviour of  $J_{rs}$  and TRM as function of grain size, *Phys. Earth planet. Inter.*, **57**, 266–283.
- Dennie, D., Elmore, R., Deng, J., Manning, E. & Pannalal, J., 2012. Palaeomagnetism of the Mississippian Barnett Shale, Fort Worth Basin, Texas, *Geol. Soc. Lond. Spec. Publ.*, **371**, 89–106.
- Dimanche, F. & Bartholome, P., 1976. The alteration of ilmenite in sediments, *Miner. Sci. Eng.*, **8**, 187–201.
- Dunlop, D.J., 2002a. Theory and application of the Day plot ( $M_{rs}/M_s$  versus  $H_{cr}/H_c$ ) 1. Theoretical curves and tests using titanomagnetite data, *J. geophys. Res.*, **107**, EPM 4-1–EPM 4-22.
- Dunlop, D.J., 2002b. Theory and application of the Day plot ( $M_{rs}/M_s$  versus  $H_{cr}/H_c$ ) 2. Application to data for rocks, sediments, and soils, *J. geophys. Res.*, **107**, EPM 5-1–EPM 5-15.
- Dunlop, D.J. & Özdemir, Ö., 1997. *Rock Magnetism: Fundamentals and Frontiers*, Cambridge Univ. Press.
- Egli, R., 2003. Analysis of the field dependence of remanent magnetization curves, *J. geophys. Res.*, **108**, 2081, doi:10.1029/2002JB002023.

- Egli, R., 2004a. Characterization of individual rock magnetic components by analysis of remanence curves. 1. Unmixing natural sediments, *Stud. Geophys. Geod.*, **48**, 391–446.
- Egli, R., 2004b. Characterization of individual rock magnetic components by analysis of remanence curves. 2. Fundamental properties of coercivity distributions, *Phys. Chem. Earth A/B/C*, **29**, 851–867.
- Egli, R., 2004c. Characterization of individual rock magnetic components by analysis of remanence curves. 3. Bacterial magnetite and natural processes in lakes, *Phys. Chem. Earth A/B/C*, **29**, 869–884.
- Egli, R., 2013. VARIFORC: An optimized protocol for calculating non-regular first-order reversal curve (FORC) diagrams, *Glob. Planet. Change*, **110**, 302–320.
- Egli, R., Chen, A.P., Winklhofer, M., Kodama, K.P. & Hornig, C.S., 2010. Detection of noninteracting single domain particles using first-order reversal curve diagrams, *Geochem. Geophys. Geosyst.*, **11**, Q01Z11, doi:10.1029/2009GC002916.
- Ellwanger, D. & Wieland-Schuster, U., 2012. Fotodokumentation und Schichtenverzeichnis der Forschungsbohrungen Heidelberg UniNord I und II, *LGRB-Inf.*, **26**, 25–86.
- Ellwanger, D., Gabriel, G., Simon, T., Wieland-Schuster, U., Greiling, R.O., Hagedorn, E.-M., Hahne, J. & Heinz, J., 2008. Long sequence of quaternary rocks in the Heidelberg Basin Depocentre, *E & G (Quat. Sci. J.)*, **57**, 316–337.
- Ellwanger, D., Gabriel, G., Hoselmann, C., Weidenfeller, M. & Wieland-Schuster, U., 2010a. Mannheim-Formation. *Litholex (online database)*. 03.11.2010 edn, <http://www.bgr.bund.de/litholex>: Federal Institute for Geosciences and Natural Resources (BGR), last accessed 13 January 2017.
- Ellwanger, D., Grimm, M., Hoselmann, C., Hottenrott, M., Weidenfeller, M. & Wieland-Schuster, U., 2010b. Iffezheim-Formation. *Litholex (online database)*. 03.11.2010 edn, <http://www.bgr.bund.de/litholex>: Federal Institute for Geosciences and Natural Resources (BGR), last accessed 13 January 2017.
- Fabian, K., 2003. Some additional parameters to estimate domain state from isothermal magnetization measurements, *Earth planet. Sci. Lett.*, **213**, 337–345.
- Fassbinder, J.W.E. & Stanjek, H., 1994. Magnetic properties of biogenic soil greigite (Fe<sub>3</sub>S<sub>4</sub>), *Geophys. Res. Lett.*, **21**, 2349–2352.
- Florindo, F. & Sagnotti, L., 1995. Palaeomagnetism and rock magnetism in the upper Pliocene Valle Ricca (Rome, Italy) section, *Geophys. J. Int.*, **123**, 340–354.
- France, D. & Oldfield, F., 2000. Identifying goethite and hematite from rock magnetic measurements of soils and sediments, *J. geophys. Res.*, **105**, 2781–2795.
- Frank, U., Nowaczyk, N. & Negendank, J., 2007. Palaeomagnetism of greigite bearing sediments from the Dead Sea, Israel, *Geophys. J. Int.*, **168**, 904–920.
- Gabriel, G., Ellwanger, D., Hoselmann, C. & Weidenfeller, M., 2008. Preface: the Heidelberg Basin Drilling Project, *Quat. Sci. J.*, **57**(3/4), 253–260.
- Gapeev, A. & Tsel'movich, V., 1983. Microstructure of synthetic titanomagnetite oxidized at high partial pressures of oxygen, *Phys. Solid Earth*, **19**, 983–986.
- Gapeev, A. & Tsel'movich, V., 1988. Microstructure and composition of multiphase-oxidized natural and synthetic titanomagnetites, *Fiz. Zemli*, **10**, 42–49.
- Garrels, R.M. & Christ, C.L., 1965. *Solutions, Minerals, and Equilibria*, Harper & Row, pp. 216–225.
- Ge, K., Williams, W., Liu, Q. & Yu, Y., 2014. Effects of the core-shell structure on the magnetic properties of partially oxidized magnetite grains: experimental and micromagnetic investigations, *Geochem. Geophys. Geosyst.*, **15**, 2021–2038.
- Gehring, A. & Hofmeister, A., 1994. The transformation of lepidocrocite during heating: a magnetic and spectroscopic study, *Clays Clay Miner.*, **42**, 409–415.
- Gendler, T., Kropáček, V. & Zapletal, R.K., 1979. Change of structure, phase composition and magnetic properties with the oxidation of titanomagnetites, *Stud. Geophys. Geod.*, **23**, 42–54.
- Gendler, T.S., Shcherbakov, V.P., Dekkers, M.J., Gapeev, A.K., Gribov, S.K. & McClelland, E., 2005. The lepidocrocite-maghemite-haematite reaction chain; I, Acquisition of chemical remanent magnetization by maghemite, its magnetic properties and thermal stability, *Geophys. J. Int.*, **160**, 815–832.
- Grygar, T., Bezduška, P., Dedeček, J., Petrovsky, E. & Schneeweiss, O., 2003. Fe<sub>2</sub>O<sub>3</sub>-Cr<sub>2</sub>O<sub>3</sub> system revised, *CERAM, Silik.*, **47**, 32–39.
- Hagedorn, E.-M., 2004. Sedimentpetrographie und Lithofazies der Jungtertiären und Quartären Sedimente im Oberrheingebiet, *Dissertation*, Universität zu Köln.
- Hagedorn, E.-M. & Boenigk, W., 2008. The Pliocene and Quaternary sedimentary and fluvial history in the Upper Rhine Graben based on heavy mineral analyses, *Neth. J. Geosci.*, **87**, 19–30.
- Hallam, D.F. & Maher, B.A., 1994. A record of reversed polarity carried by the iron sulphide greigite in British early Pleistocene sediments, *Earth planet. Sci. Lett.*, **121**, 71–80.
- Heisz, S. & Hilscher, G., 1987. The origin of graduated demagnetization curves of Nd · Fe · B magnets, *J. Magn. Magn. Mater.*, **67**, 20–28.
- Heller, F. & LIU, T.-S., 1986. Palaeoclimatic and sedimentary history from magnetic susceptibility of loess in China, *Geophys. Res. Lett.*, **13**, 1169–1172.
- Heslop, D. & Dillon, M., 2007. Unmixing magnetic remanence curves without a priori knowledge, *Geophys. J. Int.*, **170**, 556–566.
- Heslop, D. & Roberts, A., 2012. Unmixing Magnetic Hysteresis Loops, *EGU General Assembly Conference Abstracts*, **3758**.
- Heslop, D., Dekkers, M., Kruiver, P. & Van Oorschot, I., 2002. Analysis of isothermal remanent magnetization acquisition curves using the expectation-maximization algorithm, *Geophys. J. Int.*, **148**, 58–64.
- Heslop, D., Roberts, A.P., Chang, L., Davies, M., Abrajvitch, A. & de Deckker, P., 2013. Quantifying magnetite magnetofossil contributions to sedimentary magnetizations, *Earth planet. Sci. Lett.*, **382**, 58–65.
- Heslop, D., Roberts, A.P. & Chang, L., 2014. Characterizing magnetofossils from first-order reversal curve (FORC) central ridge signatures, *Geochem. Geophys. Geosyst.*, **15**, 2170–2179.
- Heywood, B.R., Mann, S. & Frankel, R.B., 1991. Structure, morphology and growth of biogenic greigite (Fe<sub>3</sub>S<sub>4</sub>), in *Proceedings of the Materials Research Society Symposium*, Cambridge Univ. Press, pp. 93–108.
- Hoffmann, V., 1992. Greigite (Fe<sub>3</sub>S<sub>4</sub>): magnetic properties and first domain observations, *Phys. Earth planet. Inter.*, **70**, 288–301.
- Hornig, C.-S. & Roberts, A.P., 2006. Authigenic or detrital origin of pyrrhotite in sediments? Resolving a paleomagnetic conundrum, *Earth planet. Sci. Lett.*, **241**, 750–762.
- Hornig, C.-S., Torii, M., Shea, K.-S. & Kao, S.-J., 1998. Inconsistent magnetic polarities between greigite- and pyrrhotite/magnetite-bearing marine sediments from the Tsailiao-chi section, southwestern Taiwan, *Earth planet. Sci. Lett.*, **164**, 467–481.
- Hoselmann, C., 2008. The Pliocene and Pleistocene fluvial evolution in the northern Upper Rhine Graben based on results of the research borehole at Viernheim (Hessen, Germany), *E & G (Quat. Sci. J.)*, **57**, 286–315.
- Hoselmann, C., Ellwanger, D., Gabriel, G., Weidenfeller, M. & Wieland-Schuster, U., 2010. Viernheim-Formation. *Litholex (online database)*. 03-11-2010 edn, <http://www.bgr.bund.de/litholex>: Federal Institute for Geosciences and Natural Resources (BGR), last accessed 13 January 2017.
- Hounslow, M.W., 1996. Ferrimagnetic C<sub>r</sub> and M<sub>n</sub> spinels in sediments: residual magnetic minerals after diagenetic dissolution, *Geophys. Res. Lett.*, **23**, 2823–2826.
- Hounslow, M.W. & Maher, B.A., 1996. Quantitative extraction and analysis of carriers of magnetization in sediments, *Geophys. J. Int.*, **124**, 57–74.
- Hounslow, M.W., Maher, B.A. & Thistlewood, L., 1995. Magnetic mineralogy of sandstones from the Lunde Formation (late Triassic), northern North Sea, UK: origin of the palaeomagnetic signal, *Geol. Soc. Lond. Spec. Publ.*, **98**, 119–147.
- Housen, B.A., Banerjee, S. & Moskowitz, B., 1996. Low-temperature magnetic properties of siderite and magnetite in marine sediments, *Geophys. Res. Lett.*, **23**, 2843–2846.

- Hu, G., Dam-Johansen, K., Wedel, S. & Hansen, J.P., 2006. Decomposition and oxidation of pyrite, *Prog. Energy Combust. Sci.*, **32**, 295–314.
- Hüsing, S., Dekkers, M., Franke, C. & Krijgsman, W., 2009. The Tortonian reference section at Monte dei Corvi (Italy): evidence for early remanence acquisition in greigite-bearing sediments, *Geophys. J. Int.*, **179**, 125–143.
- Jiang, W.-T., Horng, C.-S., Roberts, A.P. & Peacor, D.R., 2001. Contradictory magnetic polarities in sediments and variable timing of neof ormation of authigenic greigite, *Earth planet. Sci. Lett.*, **193**, 1–12.
- Johnson, N.M., Jordan, T.E., Johnsson, P.A. & Naeser, C.W., 1986. Magnetic polarity stratigraphy, age and tectonic setting of fluvial sediments in an eastern Andean foreland basin, San Juan Province, Argentina, in *Foreland Basins*, pp. 63–75, eds Allen, P.A. & Homewood, P., Blackwell Publishing Ltd.
- Just, J., Dekkers, M.J., Dobeneck, T., Hoesel, A. & Bickert, T., 2012. Signatures and significance of aeolian, fluvial, bacterial and diagenetic magnetic mineral fractions in Late Quaternary marine sediments off Gambia, NW Africa, *Geochem. Geophys. Geosyst.*, **13**, Q0A002, doi:10.1029/2012GC004146.
- Kądziałko-Hofmokr, M., Jeleńska, M., Delura, K. & Bylina, P., 2010. Magnetic mineralogy and paleomagnetism of serpentinized ultramafic rocks from the Braszowice-Brzeźnica fragment of sudetic paleozoic ophiolite, *Acta Geophys.*, **58**, 269–299.
- Kao, S.-J., Horng, C.-S., Roberts, A.P. & Liu, K.-K., 2004. Carbon–sulfur–iron relationships in sedimentary rocks from southwestern Taiwan: influence of geochemical environment on greigite and pyrrhotite formation, *Chem. Geol.*, **203**, 153–168.
- Karlin, R. & Levi, S., 1983. Diagenesis of magnetic minerals in recent haemipelagic sediments, *Nature*, **303**, 327–330.
- Kempf, O., Matter, A., Burbank, D. & Mange, M., 1999. Depositional and structural evolution of a foreland basin margin in a magnetostratigraphic framework: the eastern Swiss Molasse Basin, *Int. J. Earth Sci.*, **88**, 253–275.
- Khor, L., Parks, T., Lincoln, F.J. & Graham, J., 1996. The distribution of contaminants and the nature of the alteration products in physically separated grains of altered ilmenites, *Aust. J. Chem.*, **49**, 847–860.
- Kind, J., Gehring, A.U., Winklhofer, M. & Hirt, A.M., 2011. Combined use of magnetometry and spectroscopy for identifying magnetofossils in sediments, *Geochem. Geophys. Geosyst.*, **12**, Q08008, doi:10.1029/2011GC003633.
- Kletetschka, G. & Wasilewski, P.J., 2002. Grain size limit for SD hematite, *Phys. Earth planet. Inter.*, **129**, 173–179.
- Kraus, M.J., 1999. Paleosols in clastic sedimentary rocks: their geologic applications, *Earth Sci. Rev.*, **47**, 41–70.
- Kraus, M.J., 2002. Basin-scale changes in floodplain paleosols: implications for interpreting alluvial architecture, *J. Sediment. Res.*, **72**, 500–509.
- Kruiver, P.P. & Passier, H.F., 2001. Coercivity analysis of magnetic phases in sapropel S1 related to variations in redox conditions, including an investigation of the S ratio, *Geochem. Geophys. Geosyst.*, **2**, 1063, doi:10.1029/2001GC000181.
- Kruiver, P.P., Dekkers, M.J. & Heslop, D., 2001. Quantification of magnetic coercivity components by the analysis of acquisition curves of isothermal remanent magnetisation, *Earth planet. Sci. Lett.*, **189**, 269–276.
- Kumar, A. & Bhalla, M., 1984. Source of stable remanence in chromite ores, *Geophys. Res. Lett.*, **11**, 177–180.
- Lawson, C.A. & Nord, G.L., 1984. Remanent magnetization of a “paramagnetic” composition in the ilmenite-hematite solid solution series, *Geophys. Res. Lett.*, **11**, 197–200.
- Leonhardt, R., 2006. Analyzing rock magnetic measurements: the RockMagAnalyzer 1.0 software, *Comput. Geosci.*, **32**, 1420–1431.
- Liu, C., Ge, K., Zhang, C., Liu, Q., Deng, C. & Zhu, R., 2011. Nature of remagnetization of Lower Triassic red beds in southwestern China, *Geophys. J. Int.*, **187**, 1237–1249.
- Liu, Q., Deng, C., Torrent, J. & Zhu, R., 2007. Review of recent developments in mineral magnetism of the Chinese loess, *Quat. Sci. Rev.*, **26**, 368–385.
- Liu, X., Shaw, J., Liu, T. & Heller, F., 1993. Magnetic susceptibility of the Chinese loess-Palaeosol sequence; environmental change and pedogenesis, *J. Geol. Soc. Lond.*, **150**(Part 3), 583–588.
- Liu, X., Shaw, J., Jiang, J., Bloemendal, J., Hesse, P., Rolph, T. & Mao, X., 2010. Analysis on variety and characteristics of maghemite, *Sci. China Earth Sci.*, **53**, 1153–1162.
- Liu, Z., Zhao, X., Wang, C., Liu, S. & Yi, H., 2003. Magnetostratigraphy of Tertiary sediments from the Hoh Xil Basin: implications for the Cenozoic tectonic history of the Tibetan Plateau, *Geophys. J. Int.*, **154**, 233–252.
- Lucifora, S., Cifelli, F., Mattei, M., Sagnotti, L., Cosentino, D. & Roberts, A.P., 2012. Inconsistent magnetic polarities in magnetite- and greigite-bearing sediments: understanding complex magnetizations in the late Messinian in the Adana Basin (southern Turkey), *Geochem. Geophys. Geosyst.*, **13**, Q10002, doi:10.1029/2012GC004248.
- Ludwig, P., Egli, R., Bishop, S., Chernenko, V., Frederichs, T., Rugele, G., Merchel, S. & Orgeira, M., 2013. Characterization of primary and secondary magnetite in marine sediment by combining chemical and magnetic unmixing techniques, *Global Planet. Change*, **110**, 321–339.
- Maher, B.A., 1988. Magnetic properties of some synthetic sub-micron magnetites, *Geophys. J.*, **94**, 83–96.
- Maher, B.A. & Hallam, D.F., 2005. Magnetic carriers and remanence mechanisms in magnetite-poor sediments of Pleistocene age, southern North Sea margin, *J. Quat. Sci.*, **20**, 79–94.
- Maksimochkin, V., Gubaidullin, R. & Gareeva, M.Y., 2013. Magnetic properties and structure of Fe<sub>2-x</sub>Mg<sub>x</sub>CrO<sub>4</sub> chromites, *Moscow Univ. Phys. Bull.*, **68**, 241–248.
- Mckenroe, S.A., Harrison, R.J., Robinson, P. & Langenhorst, F., 2002. Nanoscale haematite-ilmenite lamellae in massive ilmenite rock: an example of ‘lamellar magnetism’ with implications for planetary magnetic anomalies, *Geophys. J. Int.*, **151**, 890–912.
- Menzies, J. & Ellwanger, D., 2015. Climate and paleo-environmental change within the Mannheim Formation near Heidelberg, Upper Rhine Valley, Germany: a case study based upon microsedimentological analyses, *Quat. Int.*, **386**, 137–147.
- Miall, A., 2013. *The Geology of Fluvial Deposits: Sedimentary Facies, Basin Analysis, and Petroleum Geology*, Springer.
- Milliken, K. & Mack, L., 1990. Subsurface dissolution of heavy minerals, Frio Formation sandstones of the ancestral Rio Grande Province, South Texas, *Sediment. Geol.*, **68**, 187–199.
- Moskowitz, B.M., Frankel, R. & Bazylinski, D., 1993. Rock magnetic criteria for the detection of biogenic magnetite, *Earth planet. Sci. Lett.*, **120**, 283–300.
- Murthy, I.V.R. & Krishnamacharyulu, S.K.G., 1994. Identification of NRM carriers in chromite ores by alternating field and thermal demagnetization studies, *Curr. Sci.*, **66**, 373–375.
- Muxworthy, A.R. & Dunlop, D.J., 2002. First-order reversal curve (FORC) diagrams for pseudo-single-domain magnetites at high temperature, *Earth planet. Sci. Lett.*, **203**, 369–382.
- Newell, A.J., 2005. A high-precision model of first-order reversal curve (FORC) functions for single-domain ferromagnets with uniaxial anisotropy, *Geochem. Geophys. Geosyst.*, **6**, Q05010, doi:10.1029/2004GC000877.
- Nilsson, A., Lee, Y.S., Snowball, I. & Hill, M., 2013. Magnetostratigraphic importance of secondary chemical remanent magnetizations carried by greigite (Fe<sub>3</sub>S<sub>4</sub>) in Miocene sediments, New Jersey shelf (IODP Expedition 313), *Geosphere*, **9**, 510–520.
- Nord, G.L. & Lawson, C.A., 1989. Order-disorder transition-induced twin domains and magnetic properties in ilmenite-hematite, *Am. Mineral.*, **74**, 160–176.
- Nowaczyk, N.R., 2011. Dissolution of titanomagnetite and sulphidization in sediments from Lake Kinneret, Israel, *Geophys. J. Int.*, **187**, 34–44.
- Ogg, J.G., Ogg, G. & Gradstein, F.M., 2016. *A Concise Geologic Time Scale: 2016*, Elsevier, pp. 203–223.
- Özdemir, Ö., 1990. High-temperature hysteresis and thermoremanence of single-domain maghemite, *Phys. Earth planet. Inter.*, **65**, 125–136.
- Pan, Y., Zhu, R., Banerjee, S.K., Gill, J. & Williams, Q., 2000. Rock magnetic properties related to thermal treatment of siderite: behavior and interpretation, *J. geophys. Res.*, **105**, 783–794.
- Passier, H., de Lange, G. & Dekkers, M., 2001. Magnetic properties and geochemistry of the active oxidation front and the youngest sapropel in the eastern Mediterranean Sea, *Geophys. J. Int.*, **145**, 604–614.

- Petersen, N. & Vali, H., 1987. Observation of shrinkage cracks in ocean floor titanomagnetites, *Phys. Earth planet. Inter.*, **46**, 197–205.
- Petersen, N., von Dobeneck, T. & Vali, H., 1986. Fossil bacterial magnetite in deep-sea sediments from the South Atlantic ocean, *Nature*, **320**, 611–615.
- Pike, C.R., Roberts, A.P. & Verosub, K.L., 1999. Characterizing interactions in fine magnetic particle systems using first order reversal curves, *J. Appl. Phys.*, **85**, 6660–6667.
- Preusser, F., 2008. Characterisation and evolution of the River Rhine system, *Neth. J. Geosci.*, **87**, 7–19.
- Price, G., 1980. Exsolution microstructures in titanomagnetites and their magnetic significance, *Phys. Earth planet. Inter.*, **23**, 2–12.
- Przyrowski, R. & Schäfer, A., 2015. Quaternary fluvial basin of northern Upper Rhine Graben, *Z. Dtsch. Ges. Geowissenschaften*, **166**, 71–98.
- Pye, K., 1981. Marshrock formed by iron sulphide and siderite cementation in saltmarsh sediments, *Nature*, **294**, 650–652.
- Ramdohr, R., 1975. Die Lagerstätten des Odenwaldes, *Aufschluß, Sonderbd.*, **27**, 235–236.
- Reinholdsson, M., Snowball, I., Zillén, L., Lenz, C. & Conley, D., 2013. Magnetic enhancement of Baltic Sea sapropels by greigite magnetofossils, *Earth planet. Sci. Lett.*, **366**, 137–150.
- Reiter, W., Elfert, S., Glotzbach, C. & Spiegel, C., 2015. Plio-Pleistocene evolution of the north Alpine drainage system: new constraints from detrital thermochronology of foreland deposits, *Int. J. Earth Sci.*, **104**, 891–907.
- Reynolds, R., Rosenbaum, J., Van Metre, P., Tuttle, M., Callender, E. & Goldin, A., 1999. Greigite (Fe<sub>3</sub>S<sub>4</sub>) as an indicator of drought—The 1912–1994 sediment magnetic record from White Rock Lake, Dallas, Texas, USA, *J. Paleolimnol.*, **21**, 193–206.
- Reynolds, R.L., 1977. Magnetic titanohematite minerals in uranium-bearing sandstones, *Open-File Report 77-355*.
- Roberts, A.P., 1995. Magnetic properties of sedimentary greigite (Fe<sub>3</sub>S<sub>4</sub>), *Earth planet. Sci. Lett.*, **134**, 236–227.
- Roberts, A.P., 2015. Magnetic mineral diagenesis, *Earth Sci. Rev.*, **151**, 1–47.
- Roberts, A.P. & Turner, G.M., 1993. Diagenetic formation of ferrimagnetic iron sulphide minerals in rapidly deposited marine sediments, South Island, New Zealand, *Earth planet. Sci. Lett.*, **115**, 257–273.
- Roberts, A.P. & Weaver, R., 2005. Multiple mechanisms of remagnetization involving sedimentary greigite (Fe<sub>3</sub>S<sub>4</sub>), *Earth planet. Sci. Lett.*, **231**, 263–277.
- Roberts, A.P., Cui, Y. & Verosub, K.L., 1995. Wasp-waisted hysteresis loops: Mineral magnetic characteristics and discrimination of components in mixed magnetic systems, *J. geophys. Res.*, **100**, 17 909–17 924.
- Roberts, A.P., Pike, C.R. & Verosub, K.L., 2000. First-order reversal curve diagrams: A new tool for characterizing the magnetic properties of natural samples, *J. geophys. Res.*, **105**, 28 461–28 475.
- Roberts, A.P., Chang, L., Rowan, C.J., Horng, C.S. & Florindo, F., 2011. Magnetic properties of sedimentary greigite (Fe<sub>3</sub>S<sub>4</sub>): An update, *Rev. Geophys.*, **49**, RG1002, doi:10.1029/2010RG000336.
- Roberts, A.P., Heslop, D., Zhao, X. & Pike, C.R., 2014. Understanding fine magnetic particle systems through use of first-order reversal curve diagrams, *Rev. Geophys.*, **52**, 557–602.
- Robertson, D. & France, D., 1994. Discrimination of remanence-carrying minerals in mixtures, using isothermal remanent magnetisation acquisition curves, *Phys. Earth planet. Inter.*, **82**, 223–234.
- Robinson, S.G., 1986. The late Pleistocene palaeoclimatic record of North Atlantic deep-sea sediments revealed by mineral-magnetic measurements, *Phys. Earth planet. Inter.*, **42**, 22–47.
- Rochette, P., Mathé, P.E., Esteban, L., Rakoto, H., Bouchez, J.L., Liu, Q. & Torrent, J., 2005. Non-saturation of the defect moment of goethite and fine-grained hematite up to 57 Teslas, *Geophys. Res. Lett.*, **32**, L22309, doi:10.1029/2005GL024196.
- Rolf, C., 2000. Das Kryogenmagnetometer im Magnetiklabor Grubenhagen, *Geol. Jahrb.*, **E52**, 161–188.
- Rolf, C., Hambach, U. & Weidenfeller, M., 2008. Rock and palaeomagnetic evidence for the Plio-Pleistocene palaeoclimatic change recorded in upper rhine graben sediments (Core Ludwigshafen Parkinsel), *Neth. J. Geosci.*, **87**, 41–50.
- Rösler, W., Metzler, W. & Appel, E., 1997. Neogene magnetic polarity stratigraphy of some fluvial Siwalik sections, Nepal, *Geophys. J. Int.*, **130**, 89–111.
- Rowan, C.J. & Roberts, A.P., 2006. Magnetite dissolution, diachronous greigite formation, and secondary magnetizations from pyrite oxidation: Unravelling complex magnetizations in Neogene marine sediments from New Zealand, *Earth planet. Sci. Lett.*, **241**, 119–137.
- Rowan, C.J., Roberts, A.P. & Broadbent, T., 2009. Reductive diagenesis, magnetite dissolution, greigite growth and paleomagnetic smoothing in marine sediments: a new view, *Earth planet. Sci. Lett.*, **277**, 223–235.
- Sagnotti, L., Roberts, A.P., Weaver, R., Verosub, K.L., Florindo, F., Pike, C.R., Clayton, T. & Wilson, G.S., 2005. Apparent magnetic polarity reversals due to remagnetization resulting from late diagenetic growth of greigite from siderite, *Geophys. J. Int.*, **160**, 89–100.
- Sagnotti, L., Cascella, A., Ciaranfi, N., Macri, P., Maiorano, P., Marino, M. & Taddeucci, J., 2010. Rock magnetism and palaeomagnetism of the Montalbano Jonico section (Italy): evidence for late diagenetic growth of greigite and implications for magnetostratigraphy, *Geophys. J. Int.*, **180**, 1049–1066.
- Scardia, G., Muttoni, G. & Sciunnach, D., 2006. Subsurface magnetostratigraphy of Pleistocene sediments from the Po Plain (Italy): constraints on rates of sedimentation and rock uplift, *Geol. Soc. Am. Bull.*, **118**, 1299–1312.
- Scheidt, S., Hambach, U. & Rolf, C., 2015. A consistent magnetic polarity stratigraphy of late Neogene to Quaternary fluvial sediments from the Heidelberg Basin (Germany): a new time frame for the Plio-Pleistocene palaeoclimatic evolution of the Rhine Basin, *Glob. Planet. Change*, **127**, 103–116.
- Schmidbauer, E., 1969. Magnetic properties of oxidized Fe-Cr spinels, *Z. Geophys. B*, **35**, 475–484.
- Schmidbauer, E., 1971. Magnetization and lattice parameters of Ti substituted Fe Cr spinels, *J. Phys. Chem. Solids*, **32**, 71–76.
- Schnabl, P. et al., 2010. Magnetic properties of high-Ti basaltic rocks from the Krušné hory/Erzgebirge MTS. (Bohemia/Saxony), and their relation to mineral chemistry, *Stud. Geophys. Geod.*, **54**, 77–94.
- Schumacher, M.E., 2002. Upper Rhine Graben: role of preexisting structures during rift evolution, *Tectonics*, **21**(1), doi:10.1029/2001TC900022.
- Schwarz, E. & Vaughan, D., 1972. Magnetic phase relations of pyrrhotite, *J. Geomagn. Geoelec.*, **24**, 441–458.
- Simon, T., 2012. Herkunft und Transport der Sedimente in der Forschungsbohrung Heidelberg UniNord, *LGRB-Inf.*, **26**, 107–118.
- Stacey, F.D. & Banerjee, S.K., 1974. *The Physical Principles of Rock Magnetism*, Elsevier.
- Stockhausen, H., 1998. Some new aspects for the modelling of isothermal remanent magnetization acquisition curves by cumulative log Gaussian functions, *Geophys. Res. Lett.*, **25**, 2217–2220.
- Tatzel, M., Dunkl, I. & Eynatten, H., 2015. Provenance of Palaeo-Rhine sediments from zircon thermochronology, geochemistry, U/Pb dating and heavy mineral assemblages, *Basin Res.*, **29**, 396–417.
- Tauxe, L. & Kent, D.V., 1984. Properties of a detrital remanence carried by haematite from study of modern river deposits and laboratory redeposition experiments, *Geophys. J. Int.*, **76**, 543–561.
- Tauxe, L., Mullender, T. & Pick, T., 1996. Potbellies, wasp-waists, and superparamagnetism in magnetic hysteresis, *J. geophys. Res.*, **101**, 571–583.
- Taylor, S.N., Lagroix, F., Rousseau, D.-D. & Antoine, P., 2014. Mineral magnetic characterization of the Upper Pleniglacial Nussloch loess sequence (Germany): an insight into local environmental processes, *Geophys. J. Int.*, **199**, 1463–1480.
- Tucker, P. & O'reilly, W., 1980. The laboratory simulation of deuteric oxidation of titanomagnetites: effect on magnetic properties and stability of thermoremanence, *Phys. Earth planet. Inter.*, **23**, 112–133.
- Turner, P., 1980. *Continental Red Beds*, Elsevier.

- Van Houten, F.B., 1968. Iron oxides in red beds, *Bull. geol. Soc. Am.*, **79**, 399–416.
- Vasiliev, I., Dekkers, M.J., Krijgsman, W., Franke, C., Langereis, C.G. & Mullender, T.A., 2007. Early diagenetic greigite as a recorder of the palaeomagnetic signal in Miocene–Pliocene sedimentary rocks of the Carpathian foredeep (Romania), *Geophys. J. Int.*, **171**, 613–629.
- Vasiliev, I., Franke, C., Meeldijk, J.D., Dekkers, M.J., Langereis, C.G. & Krijgsman, W., 2008. Putative greigite magnetofossils from the Pliocene epoch, *Nat. Geosci.*, **1**, 782–786.
- Verwey, E.J.W., 1935. The crystal structure of  $\gamma$ -Fe<sub>2</sub>O<sub>3</sub> and  $\gamma$ -Al<sub>2</sub>O<sub>3</sub>, *Z. Kristallogr.*, **91**, 65–69.
- Weaver, R., Roberts, A.P. & Barker, A.J., 2002. A late diagenetic (syn-folding) magnetization carried by pyrrhotite: implications for paleomagnetic studies from magnetic iron sulphide-bearing sediments, *Earth planet. Sci. Lett.*, **200**, 371–386.
- Wedel, J., 2008. Pleistocene molluscs from research boreholes in the Heidelberg Basin, *E & G (Quat. Sci. J.)*, **57**, 382–402.
- Wehland, F., Stancu, A., Rochette, P., Dekkers, M. & Appel, E., 2005. Experimental evaluation of magnetic interaction in pyrrhotite bearing samples, *Phys. Earth planet. Inter.*, **153**, 181–190.
- Weidenfeller, M. & Knipping, M., 2008. Correlation of Pleistocene sediments from boreholes in the Ludwigshafen area, western Heidelberg Basin, *E & G (Quat. Sci. J.)*, **57**, 270–285.
- Weidenfeller, M., Ellwanger, D., Gabriel, G., Hoselmann, C. & Wielandt-Schuster, U., 2010. Ludwigshafen-Formation. *Litholex (online database)*. 02.11.2010 edn, <http://www.bgr.bund.de/litholex>: Federal Institute for Geosciences and Natural Resources (BGR), last accessed 13 January 2017.
- Westerhoff, W.E., Kemna, H.A. & Boenigk, W., 2008. The confluence area of Rhine, Meuse, and Belgian rivers: Late Pliocene and Early Pleistocene fluvial history of the northern lower Rhine Embayment, *Neth. J. Geosci.*, **87**, 107–125.
- Wilkin, R. & Barnes, H., 1997. Formation processes of framboidal pyrite, *Geochim. Cosmochim. Acta*, **61**, 323–339.
- Wilson, G.S. & Roberts, A.P., 1999. Diagenesis of magnetic mineral assemblages in multiply redeposited siliciclastic marine sediments, Wanganui Basin, New Zealand, *Geol. Soc. Lond. Spec. Publ.*, **151**, 95–108.
- Winklhofer, M., Chang, L. & Eder, S.H., 2014. On the magnetocrystalline anisotropy of greigite (Fe<sub>3</sub>S<sub>4</sub>), *Geochem. Geophys. Geosyst.*, **15**, 1558–1579.